Dynamic predictability of intraseasonal variability associated with the Asian summer monsoon

By D. E. WALISER[1]*, W. STERN[2], S. SCHUBERT[3] and K. M. LAU[4]

[1]*Institute for Terrestrial and Planetary Atmospheres, State University of New York, USA*
[2]*Geophysical Fluid Dynamics Laboratory, Princeton University, USA*
[3]*Data Assimilation Office, Goddard Space Flight Center, NASA, Greenbelt, USA*
[4]*Climate and Radiation Branch, Goddard Space Flight Center, NASA, Greenbelt, USA*

SUMMARY

The objective of this study is to estimate the limit of dynamical predictability for the tropical intraseasonal oscillation (ISO) associated with the Asian summer monsoon. Ensembles of 'twin' predictability experiments were carried out with the National Aeronautics and Space Administration Goddard Laboratory for the Atmospheres atmospheric general circulation model using specified annual cycle sea surface temperatures. Initial conditions were taken from a 10-year control simulation during periods of strong ISO activity identified via extended empirical orthogonal function analysis of 30–90 day band-passed tropical rainfall. From this analysis, 21 cases were chosen for each of four distinct phases of the ISO cycle, making 84 cases in total. Two different sets of small random perturbations were added to these 84 initial states. Simulations were then performed for 90 days from each of these 168 perturbed initial conditions. A measure of potential predictability was constructed based on a ratio of the signal associated with the ISO, in terms of rainfall or 200 hPa velocity potential (VP200), and the mean-square difference between sets of twin forecasts. This ratio indicates that the limit of predictability for this model's ISO extends out to about 25 days for VP200 and to about 15 days for rainfall. The predictability measure shows modest dependence on the strength of the ISO events, with stronger events having a greater limit of predictability by a few days. It also exhibits a dependence on the phase of the ISO, with greater predictability for the convective phase at short ($\lesssim 5$ days) lead times and for the suppressed phase at longer ($\gtrsim 15$ days) lead times. The implications of these results as well as their associated model and analysis caveats are discussed.

KEYWORDS: Climate prediction   Madden–Julian Oscillation   Numerical weather forecast

1. INTRODUCTION

Efforts to predict monsoon variations span more than a century. For the most part these have consisted of empirical methods to predict anomalous seasonal rainfall using the values of one or more predictors (e.g. the position of the 500 hPa subtropical ridge, the southern oscillation state or tendency, Himalayan snow cover) established one or two seasons prior to the onset of the monsoon†. Whilst such methods have shown indications of exhibiting useful skill in a hindcast setting, they continue to have a number of shortcomings and have yet to demonstrate real operational skill (DelSole and Shukla 2002). Their most notable shortcomings are that the predictor–predictand relationships are not stationary (e.g. Parthasarathy *et al.* 1991; Hastenrath and Greischar 1993; Kumar *et al.* 1999) and the methods generally do not account for regional variability (e.g. Prasad and Singh 1992, 1996; Parthasarathy *et al.* 1993) or onset and break conditions (e.g. Kung and Sharif 1980, 1982; Kershaw 1988; Bansod *et al.* 1991).

Dynamical methods for predicting seasonal monsoon variations have also been explored (e.g. Pasch 1981; Shukla 1985a; Fennessy *et al.* 1994; Sperber *et al.* 2001).

---

* Corresponding author: Institute for Terrestrial and Planetary Atmospheres, Endeavour Hall #205, State University of New York, Stony Brook, New York 11794-5000, USA. e-mail: duane.waliser@sunysb.edu

† Including but not limited to: Blanford (1884); Walker (1923, 1924, 1928, 1933); Walker and Bliss (1932); Banerji (1950); Normand (1953); Jagannathan (1960); Banerjee *et al.* (1978); Kung and Sharif (1980, 1982); Shukla and Paolino (1983); Mooley *et al.* (1986); Hastenrath (1987); Shukla and Mooley (1987); Thapliyal and Kulshrestha (1992); Hastenrath (1995); Krishna Kumar *et al.* (1995); Rajeevan *et al.* (1998); Guhathakurta *et al.* (1999); Sahai *et al.* (2000).
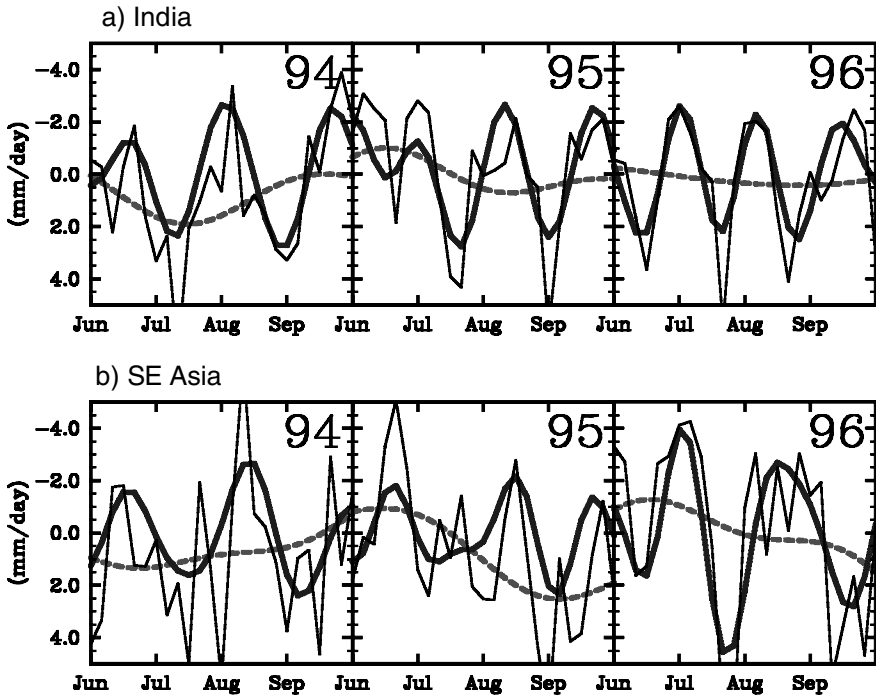
Figure 1.   June through September anomalous rainfall data for the years 1994, 1995 and 1996 for: (a) India, and (b) south-east Asia. The rainfall data are pentad values from Xie and Arkin (1997). The thin grey lines are pentad anomaly values, the thick black lines are 30–90 day band-passed values, and the dotted lines are 90-day low-pass values. The data plotted for India are the domain averages of the data grid points lying within India. The data plotted for south-east Asia are the domain averages of the data grid points encompassing the majority of Thailand, Laos, Cambodia, Vietnam and Indonesia.

Thus far, however, no operational benefit has been realized by dynamical predictions of low-frequency monsoon variations. This is due to poor representation by general circulation models (GCMs) of the essential scales of variability associated with the monsoon, in combination with the perceived mix of predictable and unpredictable components of the monsoon (e.g. Sperber *et al.* 2000; Sperber *et al.* 2001). With regard to the former, a recent study by Kang *et al.* (2002a,b) shows that present-day atmospheric GCMs (AGCMs) are unable to simulate the most fundamental features of anomalous interannual conditions of the monsoon even when the sea surface temperature (SST) is prescribed from observations. The results of this study echo the findings of Sperber and Palmer (1996) that showed that a suite of state-of-the-art models was largely unable to hindcast seasonal monsoon variability with any useful skill.

From the discussion above, it is still not clear whether seasonal monsoon forecasts suffer primarily from poor models (statistical or dynamical) or if they are also predisposed to failure due to an inherently unpredictable nature of the monsoon on seasonal to interannual time-scales. Given these challenges, the present study is motivated by the viewpoint that predictions of the intraseasonal oscillations (ISOs) associated with the monsoon may be at least as (if not more) valuable to pursue as predictions of the lower-frequency fluctuations (e.g. seasonal departures). As an illustration of the relative roles that intraseasonal and interannual time-scales play in monsoon variability, Fig. 1 compares total pentad anomaly, intraseasonal (30–90 day), and interannual (>90 day) fluctuations in area-averaged rainfall over India and south-east Asia for the 1994, 1995

and 1996 monsoons. From this figure, it is apparent that the intraseasonal time-scale is a recurrent form of variability within the monsoon. When this time-scale is active, it comprises a significant fraction of the total anomalous variability (e.g. Sperber *et al.* 2000) and, most importantly, it is primarily responsible for characterizing the onsets and break periods of the monsoon (e.g. Yasunari 1979, 1980; Cadet 1986; Lau and Chan 1986; Webster *et al.* 1998).

Apart from the significant influences that ISO variability over the Indian and southeast Asian sectors has on the monsoon, there are also important downstream influences that arise from the ISO. For example, ISO convective activity has been linked to northern hemisphere (NH) summertime precipitation and circulation variability over Mexico (Mo 2000b) and the Pacific–South America sector (Mo and Higgins 1998). Recently, studies have also shown that particular phases of the ISO can be more favourable than others in regard to the development of tropical storms/hurricanes in both the Atlantic and Pacific sectors (Maloney and Hartmann 2000a,b; Mo 2000a; Higgins and Shi 2001).

As influential as the ISO is on the character and evolution of the monsoon, as well as the downstream processes mentioned above, a fundamental question yet to be adequately addressed concerns its theoretical limit of predictability. For example, it is well known that useful skill associated with deterministic prediction of most 'weather' phenomena is limited to about 6–10 days (e.g. Thompson 1957; Lorenz 1965, 1982; Palmer 1993; van den Dool 1994). Similarly, it has been found that the likely limit of predictability for the El Niño Southern Oscillation (ENSO) is on the order of 12–18 months (e.g. Cane *et al.* 1986; Graham and Barnett 1995; Kirtman *et al.* 1997; Barnston *et al.* 1999). However, it is yet to be determined what the corresponding metric is for NH summertime ISO events. Its time-scale alone suggests that useful predictive skill might exist out to at least 15–25 days and maybe longer. Support for this suggestion comes from a statistical predictive model of the ISO, which indicates useful skill out to at least 15–20 days lead time (see Waliser *et al.* 1999b; cf. Lo and Hendon (2000) and Mo (2001) for additional analogues for NH wintertime ISO variability). However, as with any statistical model, these models are limited in the totality of the weather/climate system they can predict, their ability to adapt to arbitrary conditions, and their ability to take advantage of known physical constraints.

Studies of dynamical prediction skill with regard to Asian summer monsoon ISO events, which could have some bearing on determining ISO predictability limits, are largely non-existent due to the generally poor simulation characteristics of intraseasonal variability by present-day AGCMs (e.g. Waliser *et al.* 2003b; cf. Slingo *et al.* (1996) for NH wintertime ISO variability). One noteworthy exception is the studies by Krishnamurti *et al.* (1990, 1992) that used a global atmospheric forecast model with initial conditions that had been filtered to only retain the 'low-frequency modes' (i.e. ISOs) of the monsoon. In their experiments, there appeared to be useful forecast skill out to around 20–30 days for selected events. An additional study by Schemm (1997) showed that the most recent version of the National Centers for Environmental Prediction medium-range forecast model's dynamic extended-range forecasts might have some skill in forecasting onset and breaks out to about 7–10 days. However, the skill limits from this latter study are likely to be underestimates of the potential predictability due to the very weak intraseasonal signature in the model (e.g. Hendon *et al.* 2000; Jones *et al.* 2000). In any case, since these studies were really measuring forecast skill of the model, their skill versus lead time estimates will be additionally hampered by the difference in phase speeds between the model and observations, and the uncertainties in the specified initial conditions. While these studies can be indicative, ascertaining an estimate of the theoretical limit of predictability for the ISO from them is not entirely appropriate.

In this study, we determine an estimate for the theoretical limit of dynamic pre-dictability of the NH summertime ISO by conducting a set of twin numerical predictabil-ity experiments (e.g. Thompson 1957; Lorenz 1965; Charney *et al.* 1966; Shukla 1985b) with a given model—one that has a reasonable representation of the ISO's space–time variability. Using this methodology, we attempt to address the following questions. What is the typical limit of predictability for the tropical MJO phenomenon? How is this limit influenced by the strength and phase of the ISO? Our study focuses on the NH summer ISO phenomenon (i.e. north-east propagating; Wang and Rui 1990; Wang and Xie 1997) and the associated implications this limit has on Asian summer monsoon pre-diction. A parallel study by Waliser *et al.* (2003a) addresses the limit of predictability for the NH winter (eastward propagating) mode of intraseasonal variability (i.e. Madden–Julian Oscillation (MJO), Madden and Julian 1994).

The next section describes the model employed for this study. Section 3 describes the experimental framework and the analysis methods. Section 4 presents the results of the experiments. Section 5 presents a summary of the results, considers the caveats of the model and analysis, and discusses the implications of this result with regards to the pre-dictability of monsoon onsets and breaks as well as other weather/climate phenomena that are influenced by the ISO.

2.   THE MODEL

The model used in these experiments is the National Aeronautics and Space Administration (NASA) Goddard Laboratory for the Atmospheres (GLA) GCM. This model was derived from an earlier version described by Kalnay *et al.* (1983). Modifications have included increased vertical resolution and numerous changes in the parametrizations of radiation, convection, cloud formation, precipitation, vertical diffusion, and surface processes (Sud and Walker 1992; Phillips 1994). The horizon-tal representation uses finite differences on a $4° \times 5°$ (latitude $\times$ longitude) energy and momentum conserving A-grid (Arakawa and Lamb 1977). The horizontal advec-tion of the atmospheric variables is accurate to fourth order (Kalnay *et al.* 1983). The vertical domain has 17 unequally spaced sigma levels extending from the surface to about 12 hPa. At every dynamical time step, a sixteenth order Shapiro (1970) filter (with time-scale 90 minutes) is applied to the prognostic fields; a Fourier filter is also used in polar latitudes. Negative moisture values are filled by 'borrowing' moisture from the level below, and from neighbouring horizontal grid boxes at the lowest vertical level. Horizontal diffusion is not included and the effects of vertical diffusion are treated by the level-2.5 second order turbulence closure model of Helfand and Labraga (1988).

Near the surface, the planetary boundary layer (PBL) is treated as an extended surface layer with a viscous sub-layer in the space between the surface and the tops of the surface roughness elements. Appropriate parametrizations are utilized to determine turbulent fluxes in the different PBL sub-regions. Both seasonal and diurnal cycles in the solar forcing are simulated with the atmospheric radiation treatment of Harshvardhan *et al.* (1987). The formulation of the convection follows the scheme of Arakawa and Schubert (1974), as implemented in discrete form by Lord and Arakawa (1980). The model orography is based on the $1° \times 1°$ topographic height data of Gates and Nelson (1975) which has been area-averaged over the $4° \times 5°$ grid boxes. The resulting orography is smoothed using a sixteenth order Shapiro (1970) filter, and a Fourier filter poleward of 60 degree latitude. Negative terrain heights resulting from the smoothing process are set to zero. Land-surface processes are simulated as in the Xue *et al.* (1991) modification of the model of Sellers *et al.* (1986).

In general, the GLA model performed very well with respect to its representation of NH winter intraseasonal variability (i.e. MJO) in the Atmospheric Model Intercomparison Project study (Slingo *et al.* 1996), being one of about three AGCMs—UKMO (UK Met Office), GLA, and CCM2 (Canadian Climate Model)—that contained variability closely resembling the observed features of the oscillation. In fact, a more rigorous comparison of the ISO in the GLA and UKMO models by Sperber *et al.* (1997) showed that of the two models, the GLA model tended to produce a better representation of the eastward propagation of convection and its associated cyclonic and anticyclonic circulation anomalies. While the above two studies focus on the NH wintertime (i.e. MJO), a recent study by Waliser *et al.* (2003b) shows that of ten AGCMs examined, the GLA model performed relatively well in regards to its simulation of NH summertime ISO variability. In addition, that study also showed that the fidelity of a model's representation of winter MJO versus summer ISO variability tends to go hand in hand. While modest improvements in the GLA simulation of the NH wintertime intraseasonal variability were obtained by incorporating a weakly coupled SST feedback (Waliser *et al.* 1999a), this study utilizes the fixed SST version of the model. A future study will report on the influences of SST coupling and interannual SST anomalies on the predictability of individual ISO events.

3. EXPERIMENTAL FRAMEWORK

As a basis for selecting initial conditions for a number of ISO forecast cases, a 10-year simulation using mean monthly climatological SSTs was performed and daily averages (four 6-hour values) of a number of fields were saved. From this simulation, ISO forecast cases were chosen based on an extended empirical orthogonal function (EEOF) analysis (Weare and Nasstrom 1982) of rainfall data from the region $32°N$ to $32°S$, 17.5 to $135°E$. This region tends to encompass most of the variability in rainfall that is associated with the ISO (e.g. Lau and Chan 1986; Wang and Rui 1990). To isolate the intraseasonal time-scale, and thus the ISO, the data were first band-passed with a (121 point) 30–90 day Lanczos filter (Duchon 1979). EEOF analysis was then performed on pentad averages of the NH 'summer' data, hereafter defined as May through October, using temporal lags from -7 to $+7$ pentads. The spatial–temporal pattern for the first EEOF mode, shown in Fig. 2, depicts the bulk characteristics of the typical cycle of the model ISO in terms of rainfall. The spatial–temporal pattern of mode 2 (not shown) exhibits a quadrature relation with mode 1, otherwise the two modes are very similar. The first (second) mode contains 5.0% (4.9%) of the band-passed variance. Note that these percentages are not just of the data itself but of the time-lagged sequences of data that were analysed within the context of an EEOF analysis.

To illustrate the degree of realism associated with the model's ISO, the same EEOF analysis was performed on 10 years (1988–97) of pentad rainfall data from Xie and Arkin (1997). The first EEOF mode (not shown) from this analysis has a very similar structure to the model EEOF mode shown in Fig. 2, although the observed mode captures slightly more variance (5.8%). Composite ISO events from the model and observations were constructed by averaging the band-passed rainfall and VP200 data for all pentads that had an EEOF mode 1 time series amplitude greater than 0.8. For the model (observations), this included 26 (21) pentads. This resulted in a composite ISO, in terms of rainfall and VP200, extending from lags -7 pentads to $+7$ pentads (similar in structure to Fig. 2). To concisely illustrate the model–data comparison, lags -7 and -6 were averaged together (to be referred to as lag -6.5), lags -5 and -4 pentads were averaged together (to be referred to as lag -4.5), and so forth, giving composite maps
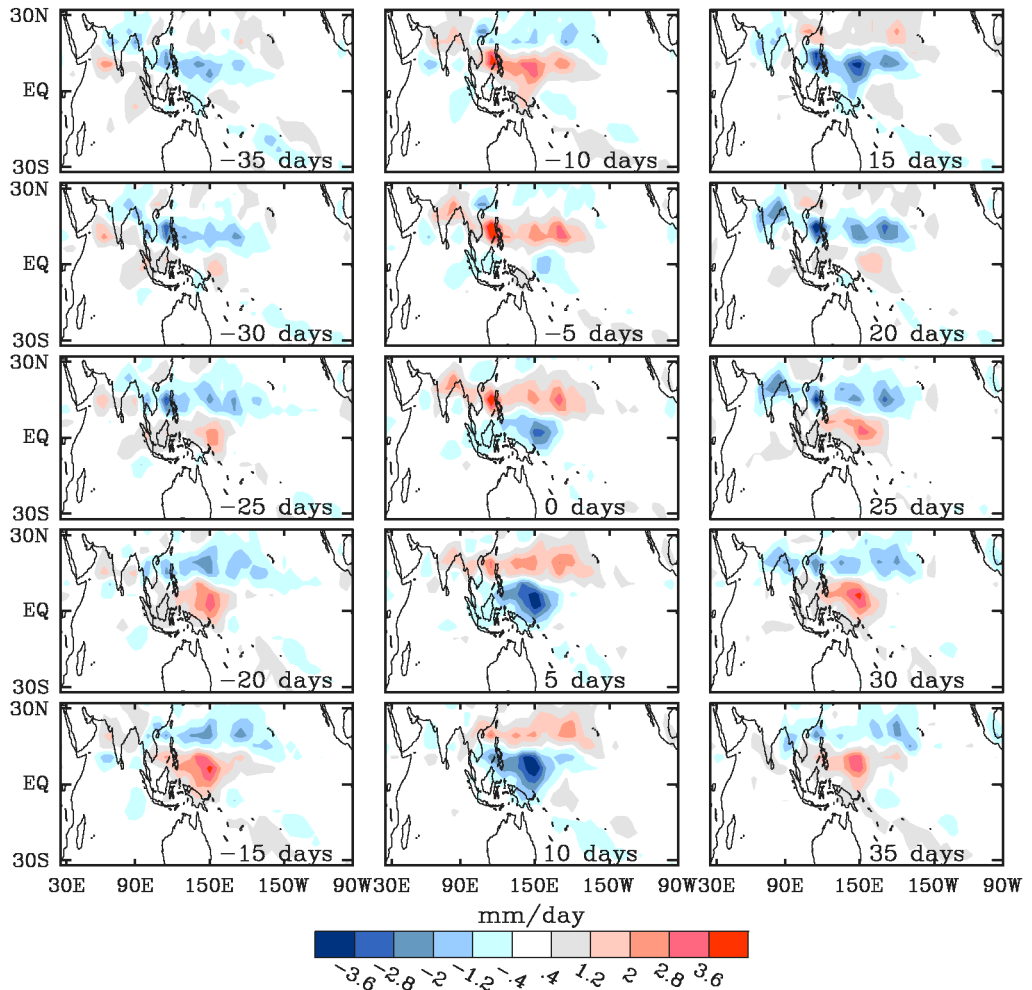
Figure 2. First mode extended empirical orthogonal function (EEOF) of filtered (30–90 days) northern hemisphere summer (May–October) model rainfall for the tropical domain shown. Time lags extend from −35 days (i.e. −7 pentads) in the upper-left to +35 days (i.e. +7 pentads) in the lower-right. See section 3 for details.

separated by 2 pentads (i.e. 10 days). The composite maps for lags of −4.5, −2.5, −0.5, +1.5 and +3.5 pentads for both the observed and model ISO composites are shown in Fig. 3. A comparison of these two life cycles shows that the model ISO has fairly realistic characteristics in terms of the space–time variability of ISO-induced rainfall and VP200. This includes the overall time-scale, the magnitude and locations of the variability, the propagation speed, etc. In comparing the two composite events, it should be kept in mind that there is no constraint in the above analysis to align the phases of the observed and modelled events. Thus the modest lead that the observed event exhibits over the modelled one is insignificant. Two of the more significant shortcomings in the model are its weaker rainfall variability in the equatorial Indian Ocean and the associated diminished response in the VP200 composites. The potential implications associated with these shortcomings are discussed in section 5.

Candidate ISO cases to use for initial conditions were chosen from the amplitude time series associated with model EEOF modes 1 and 2; these time series are shown
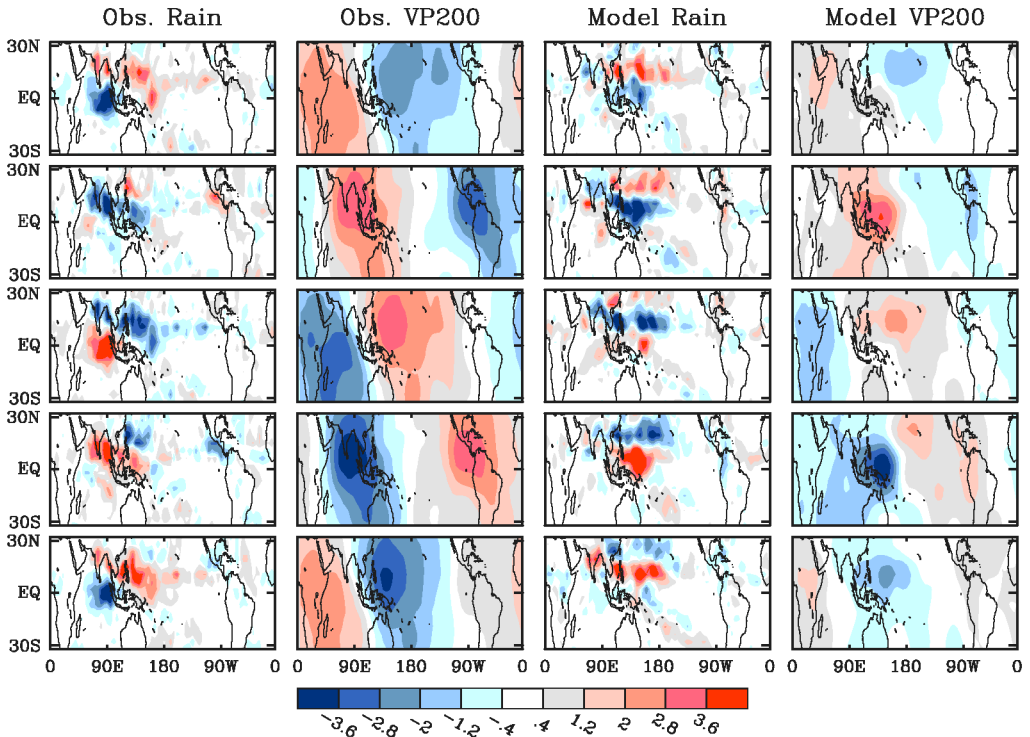
Figure 3. Composite northern hemisphere summer intraseasonal oscillations from observations (left) and the model (right). Sequential maps are separated by 10 days. Units for rainfall are mm day^{-1}, and for 200 hPa velocity potential (VP200) are 10^6m^{2}s^{-1}. See section 3 for a description of their construction.

in Fig. 4. Given that these models capture the propagating nature of the ISO, selecting periods when the amplitude of these time series is large will tend to capture strong, propagating ISO events. For the purpose of selecting specific days for initial conditions, these two pentad time series were interpolated to daily values. The two series have maximum correlation (0.97) at a lag of ±12 days, indicating a dominant period of about 48 days, consistent with what is indicated in the EEOF shown in Fig. 2. The corresponding result for the first two EEOF modes of the observed pentad data described above is 0.85 at a lag of about ±2.5 pentads ($\sim$12 days). Note that when the mode 1 time series is negative (positive), rainfall tends to be high across a region extending from the maritime continent to the equatorial western Pacific (India to south-east Asia) region, and when the mode 2 time series is negative (positive), rainfall tends to be high across a region extending from the Bay of Bengal to the South China Sea and on to the western tropical Pacific Ocean (southern China to the north-west tropical Pacific Ocean). Thus, by selecting periods of both positive and negative values of these two series, four separate 'phases' of the ISO can be distinguished based on the position of the heating. For each of these four phases the 21 cases with the greatest amplitudes were selected. These cases are highlighted in Fig. 4. Figure 5 shows the composite rainfall for the 21 initial conditions selected for each of the four ISO phases.

Two perturbations were performed for the 84 cases selected (21 cases in each of four ISO phases). The perturbation initial conditions were determined in a fairly simplistic manner. Given the day of the month of the initial condition, day-to-day root-mean-square (RMS) differences were computed for the model's four prognostic variables
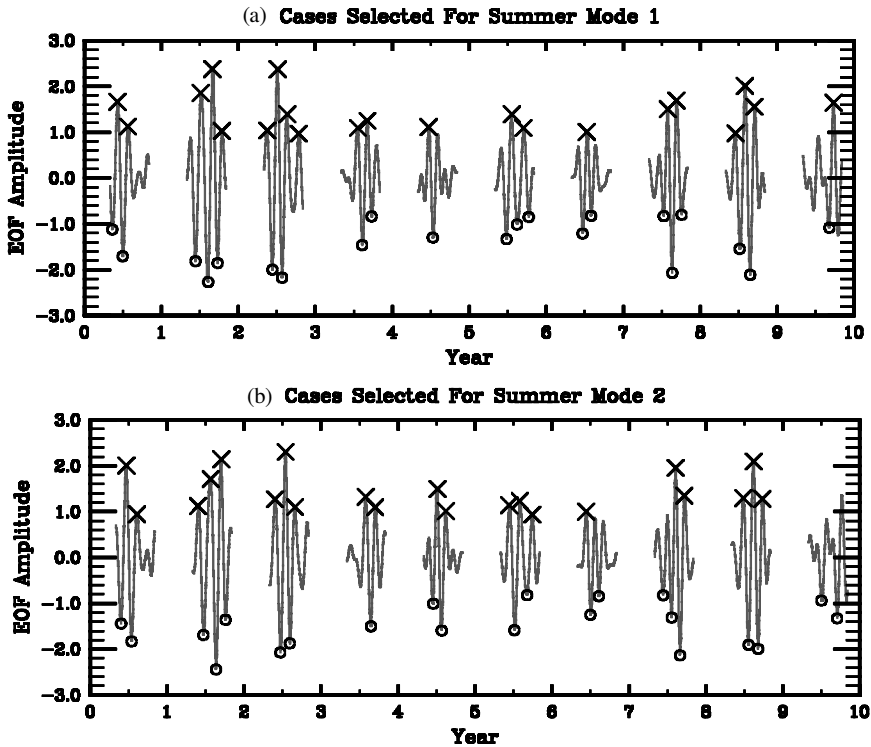
Figure 4. Amplitude time series for: (a) the first, and (b) the second extended empirical orthogonal function (EEOF) of filtered (30–90 days) northern hemisphere summer model rainfall. The X's and O's represent the time periods selected for initial conditions for the intraseasonal oscillations case. See section 3 for details.

(velocity components u, v, temperature T, and humidity q) on sigma surfaces for that particular month. These RMS values were then multiplied by a random number scaled between -0.1 and 0.1 for the first set of perturbations and -0.2 and 0.2 for the second set. These 'errors' were then added to the original initial condition's prognostic values to produce an alternative initial condition. The different size of the error between the first and second sets is used to provide some information on the sensitivity of the predictability to the size of the initial condition perturbation. The use of the RMS daily differences was meant to assign larger uncertainty in regions where the atmosphere is more variable and thus likely to be subject to more uncertainty in initialization.

For each alternative initial condition, the model was integrated for 90 days. To isolate the ISO phenomena and distinguish its predictability from high-frequency weather fluctuations, the 120 days of model simulation prior to the initial condition was combined with the 90-day 'forecasts' and the result band-pass filtered using the same 30–90 day filter described above. A triangular taper 40 days long was applied at either end of these 210-day series.

4. RESULTS

While there are a number of ways to define predictability for atmospheric phenomena (e.g. Shukla 1985b; Stern and Miyakoda 1995; Anderson and Stern 1996; Yang *et al.* 1998; Schneider and Griffies 1999), the approach taken here attempts to make a relatively conservative estimate of the limit of predictability for the ISO. When the ISO
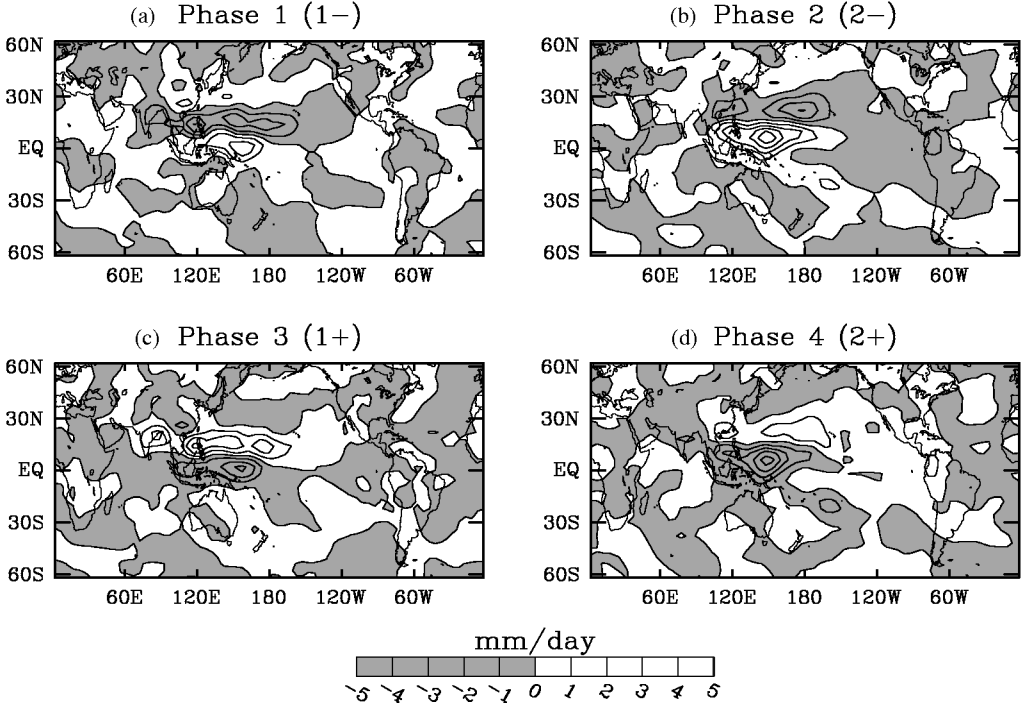
Figure 5. Composite filtered (30–90 days) rainfall anomalies for the 15 initial conditions selected to represent four 'phases' of the intraseasonal oscillations (ISO): (a) Phase 1 (1−), the average rainfall anomaly from the 21 initial conditions indicated by the O's in Fig. 4(a) (i.e. Mode 1); (b) Phase 2 (2−), the average rainfall anomaly from the 21 initial conditions indicated by the O's in Fig. 4(b) (i.e. Mode 2); (c) and (d) are as (a) and (b) but for the 21 initial conditions indicated by the X's in Figs. 4(a) and (b), respectively. The headings indicate the rainfall extended empirical orthogonal function (EEOF) mode and sign (e.g. 1+ indicates EEOF mode one amplitude time series greater than zero).

is active, it tends to exhibit an oscillatory form in which the magnitude of the oscillation can be said to represent the 'signal'. Of interest here is how long before the forecast 'errors' resulting from the imprecise initial conditions grow to be as large as this signal. Schematically, this is illustrated in Fig. 6. Thus for the ISO cases selected, we examine how the mean forecast error compares (versus lead time) to their mean signal. The signal for a given case is defined as the variance within a sliding window (of width $2L + 1$) that is large enough to encompass a complete ISO event:

$$\sigma_{\text{S}ij}^2 = \frac{1}{2L + 1} \sum_{\tau=-L}^{L} (X_{i,j+\tau}^0)^2. \tag{1}$$

The forecast error for a given case and lead time is defined as the mean-square difference between the perturbed case and the control case:

$$\sigma_{\text{E}ijk}^2 = (X_{ij}^k - X_{ij}^0)^2. \tag{2}$$

In the above equations: X is the geophysical quantity being analysed (e.g. filtered VP200), i is the ISO case, j is the day number relative to the initial forecast date (referred to here as forecast day as well as lead time), and k is the perturbation number with X^0 representing the control case. The mean signal and mean-square forecast error
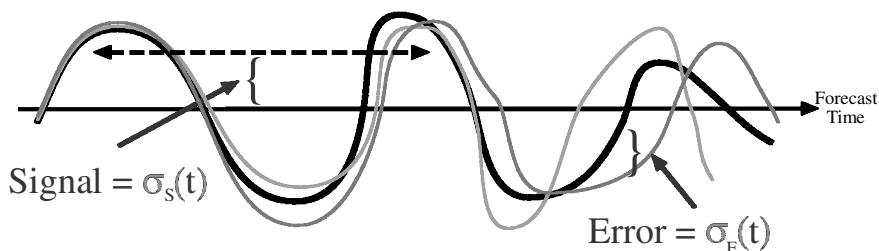
Figure 6. Schematic depiction of the evolution of a Madden–Julian Oscillation case versus forecast time for a control forecast (thick line) as well as two forecasts with perturbed initial conditions (thin lines). The forecast error at any given time, $\sigma_E(t)$, between the control forecast and a perturbed forecast is the difference between the two time series. The signal of the intraseasonal oscillation (ISO) case at any given time, $\sigma_S(t)$, is represented as the running variance of the time series (shown here in terms of standard deviation), where the averaging length is long enough to encompass a typical ISO period. Thus the 'signal' is a representation of the overall amplitude of a given ISO event. See Eqs. (1)–(4) and section 4.

for a given set of N cases are then simply defined as:

$$\overline{\sigma_{S_j}^2} = \frac{1}{N} \sum_{i=1}^{N} \sigma_{S_{ij}}^2, \tag{3}$$

$$\overline{\sigma_{E_j}^2} = \frac{1}{2N} \sum_{k=1}^{2} \sum_{i=1}^{N} \sigma_{E_{ijk}}^2. \tag{4}$$

In the above equations, N is typically set to 21 (e.g. 21 cases for a particular phase of the ISO) or 84 (all ISO cases), and L is set to 25. In addition, given that the two sets of perturbations ($k = 1, 2$) are distinguished by the different size of the initial perturbations, the error growth for these two sets can be calculated separately in Eq. (4) by averaging only over $k = 1$ in one case, and only over $k = 2$ in the second. Using the above definitions, a predictability ratio can be defined as:

$$\overline{\sigma_{S_j}^2} / \overline{\sigma_{E_j}^2}, \tag{5}$$

with the implication that at early lead times this ratio will be much larger than unity, and at the point it becomes of order unity little predictability remains. Note that an alternative to the above approach would be to perform a much larger ensemble of forecasts for one, or a few, cases and compare the ensemble spread at any given lead time to the size of the mean signal. This represents a more typical approach of comparing signal to 'noise'. However, given limited computing resources, this approach drastically reduces the number of cases that can be represented in the analysis. For example, given the same number of simulations, only three cases could be examined if the ensemble size was set to ten. Since it is unknown how variable the predictability of the ISO might be from one case to the next, selecting one or a few cases to be representative might prove difficult. For this reason, we opted for the approach outlined above. However, it is worth noting that in conjunction with the analogous study for the NH wintertime (i.e. MJO, Waliser *et al.* 2003a), a 15-member ensemble of forecasts (i.e. $k = 1 \ldots 15$) for a single MJO event exhibited predictability characteristics similar to a small ensemble (i.e. $k = 1, 2$) for a large number of MJO events (i.e. $N = 15$).

Figure 7 illustrates the temporal evolution of VP200 for the selected cases (i.e. $N = 21$ for each case) for a domain over the South China Sea (see smaller box in Fig. 11). This region has been chosen due to the large amount of ISO variability
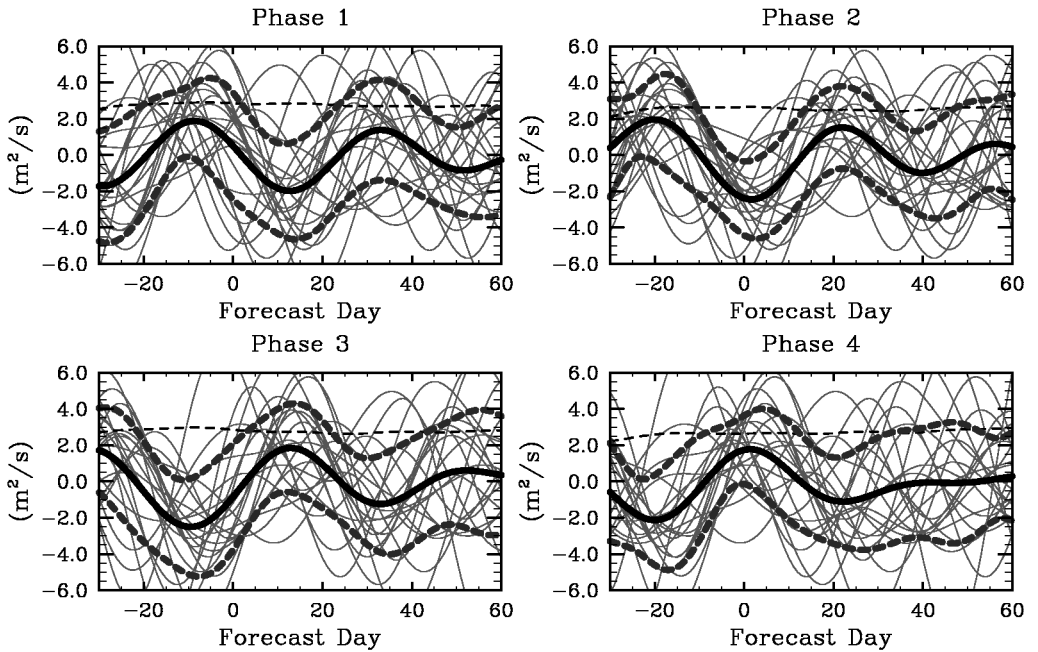
Figure 7. The evolution of filtered (30–90 day) 200 hPa velocity potential (VP200) over the region 8–20°N, 107.5–132.5°E depicted by the thin solid lines (see smaller box in Figs. 10 and 11) for the selected intraseasonal oscillation (ISO) cases. The headings indicate the phase of the ISO cases which, when considered with Fig. 5, indicates the spatial structure of the ISO-related convection that was typical at the start of the forecasts. The thick solid lines are ensemble means of the 21 time series in each phase; thick dotted lines are the mean values plus and minus one standard deviation; thin dotted lines are the square root of the mean ISO signal as defined by Eq. (3). VP200 values have been scaled by 10^{-6}.

exhibited by the model in association with the south-east Asian monsoon and due to its proximity to a number of highly populated areas. This figure illustrates the VP200 evolution for the cases that were selected to represent four different phases of the ISO. In a general sense, the selection process appears to have selected robust ISO events and categorized them into four separate phases. However, it is interesting to note that the same selection procedure was applied to the NH winter ISO mode (i.e. MJO) in Waliser *et al.* (2003a), and the coherence with respect to phase and amplitude of the cases selected for each of the four phase categories in that case was significantly greater. This suggests that the variability associated with the NH summer mode of the model has a more complicated modal structure and associated space–time structure than that associated with the winter mode.

Figure 8 shows the mean signal (Eq. (3)) and mean-square forecast errors (Eq. (4)) versus lead time for VP200 and rainfall for all the selected cases ($N = 168$) for the model grid point in the centre of the region discussed above, together with 95% confidence limits. As expected, the values of the mean signals remain roughly constant through the period shown. However, since the ISO cases were chosen based on maxima found in the EEOF amplitude time series, a slight decrease in the signal is exhibited away from forecast day 0 for the ISO cases. In addition, part of the decrease in the signal at long lead times ($\gtrsim 45$ days) is due to the application of the triangular taper before band-passing (see section 3).

Of interest here is the lead time when the mean forecast error and the mean signal are equal. For this particular location, this tends to occur at about 30 days for
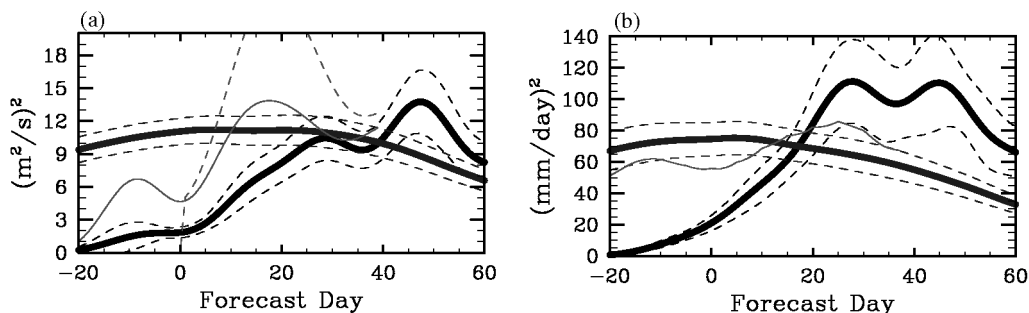
Figure 8. (a) Mean-squared forecast error (Eq. (4)) for the (30–90 day) filtered 200 hPa velocity potential (VP200) over the region 12–16°N and 117.5–122.5°E (model grid point at centre of smaller box in Figs. 10 and 11) for all the selected intraseasonal oscillation (ISO) cases ($N = 168$), shown by the thick solid black line that increases with forecast time; the mean ISO signal (Eq. (3)) is also shown, by the thick solid black line that is roughly constant with forecast time; 95% confidence limits for these two quantities using a Students *t*-test are given by the thin dotted lines; additionally the mean-squared forecast errors for two different types of persistence forecasts (see section 4 for more details) are given by the thin grey line. (b) As (a) but for rainfall, except that the thin grey line in this case gives the mean-squared forecast errors for an empirical forecast method based on the canonical ISO pattern depicted in Fig. 2 (see section 4 for more details). VP200 values have been scaled by 10^{-12}.

VP200 and 18 days for rainfall. Note however that the size of the confidence limits indicates that these values may vary from 20–40 days for VP200 and 15–20 days for rainfall. In addition, given that the observed and modelled ISO exhibits significant spatial–temporal variability (e.g. Figs. 2, 3), it is likely that the modelled (and observed) ISO predictability characteristics depend on location. Thus the intention of showing and discussing these plots is mainly to provide information on the limit of predictability in a ISO-relevant area but also to illustrate the sort of dependencies that there might be in terms of ISO strength, the ensemble size examined etc., and to illustrate the overall behaviour of the signal and forecast error—the two components that make up the predictability measure described above.

It is worth noting that the forecast errors shown in Fig. 8 are not zero at 0 days lead due to the use of the band-pass filter to isolate the ISO phenomena. The application of such a filter introduces useful information into the early forecast period from the period prior to the forecast, and erroneous information into the period prior to the forecast from the forecast itself. It is important to point out at this stage that the determination of how one measures forecast skill, and/or produces forecasts of the MJO/ISO given its intraseasonal time-scale, is in itself a topic of current research. One cannot use daily data or the forecast analysis will end up addressing weather variations. There is a near-necessity for the use of a filtering process to isolate the MJO/ISO; most empirical MJO/ISO forecast studies (Waliser *et al.* 1999b; Lo and Hendon 2000; Mo 2001; Wheeler and Weickmann 2001) and hindcast MJO forecast skill studies (Hendon *et al.* 2000; Jones *et al.* 2000) have had to grapple with this issue and in no case have the methods been completely satisfying.

In addition to the mean-square errors associated with the dynamical model, mean-square forecast errors for other empirical forecast schemes are given in Fig. 8. In the VP200 panel, two forms of persistence are also shown. For these persistence forecasts, the day 0 daily averaged value was persisted for 90 days. The data were then band-passed in the same manner as for the dynamical forecasts. In one case, the day 0 value from this operation is simply persisted through the forecast period. In the second case, the actual values resulting from the band-pass operation are used (hereafter 'tidal' forecast). This latter case shows some improvement in skill over the former (~4 days) due the use

of the information associated with the band-pass operation; this has some analogy to the application of harmonic analysis to tidal prediction.

It is understood that persistence, even its 'enhanced' form as just described, is not well suited to an 'oscillating' phenomena, and thus a second form of empirical prediction is shown in the rainfall panel of Fig. 8. In this case, the values associated with the 'tidal' forecasts described above were projected onto the first two EEOF modes of rainfall (mode 1 is shown in Fig. 2). Note that the pentad-based EEOF modes were first interpolated to daily values and thus subsequently extend from -37 to $+37$ days lag. The amplitude values obtained from these projections were then multiplied by the EEOF vectors themselves, and the values obtained after day 0 and up to a lead time of 37 days were used as a forecast. As is evident from the figure, this method's skill at lead times around 15 days is comparable to, although slightly less than, the dynamical model, and not too different from the sort of forecast skill that has been obtained from the empirical methods cited above. However, this method shows very poor skill at short lead times from to two factors: (i) the problem noted above, in this case regarding computation of the EEOF projection in light of the fact there is only estimated data after the starting period, and (ii) the low order EOFs are considerably smoother in space leading to higher RMS. For example, in comparing two numerical forecasts at early lead times it is likely that some of the spatial details may actually agree. However, since the EEOF-based forecast is relatively smooth in space, these spatial details will not agree since they do not exist in the EEOF—thus leading to higher RMS errors. The main point of the above exercise is to show evidence that a simple empirical scheme developed from the model data does exhibits skill, at least at long leads, that is similar to empirical model efforts that were more directly focused on this endeavour using observations (see citations above), and that the dynamical model appears to exhibit a predictive skill that is not too dissimilar from an empirical approach (albeit one that could likely be improved upon).

Figure 9 illustrates how the manner and degree that the predictability characteristics discussed above depend on ISO strength. In this case, the forecasts were separated into two groups: those associated with the strongest ten, and those associated with the weakest ten ISO cases as measured by the EEOF amplitudes shown in Fig. 4. Thus, of the 21 total cases selected for each of the four phases, the strong (weak) classification included the ten cases with the highest (lowest) EEOF amplitudes. Thus the predictability characteristics in Fig. 9 are based on N values equal to 80 (ten cases of four phases each with two perturbations). These plots indicate that through a combination of smaller error growth around 15–20 days and a larger signal for the strong cases as compared to the weak cases, the stronger ISO cases appear to exhibit more predictability than the weaker ISO cases. However, it is important to keep in mind that the uncertainty levels are considerably larger for this sample size. The above result is not entirely unexpected, since in the limit that there is little or no ISO activity exhibited in the system (and thus little intraseasonal variability), there would be no coherent signal to exploit to provide skill for extended-range predictions. In such an extreme case, the 'ISO forecast skill' would largely be dictated by the skill associated with long-lead tropical 'weather' prediction. The companion NH wintertime study of the MJO by Waliser *et al.* (2003a) found that the model (intraseasonal) forecast skill associated with periods nearly absent of MJO activity (referred to as 'null' cases in that study) was nearly the same as that for the model's tropical 'weather'. Additional analysis of this issue will be discussed further below.

To illustrate the spatial dependence of the results associated with Fig. 8, Fig. 10 shows the ISO signal (Eq. (3)) and mean-square forecast error (Eq. (4)) for VP200 at
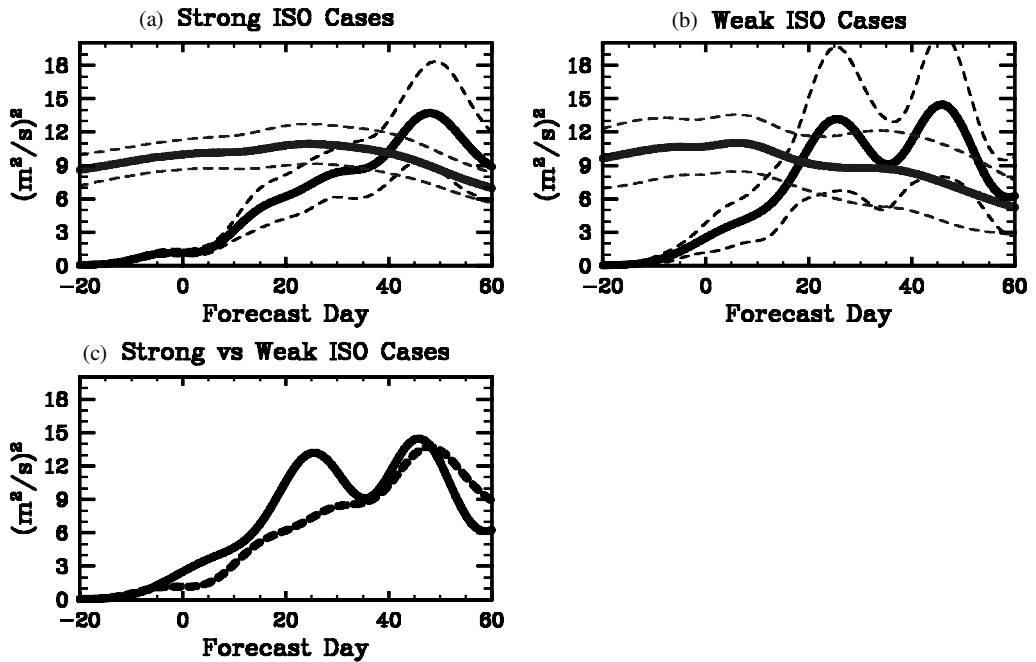
Figure 9.   (a) As Fig. 8(a) but based on forecasts using the strongest ISO cases ($N = 80$, see section 4); (b) as (a) but for the weakest ISO cases; (c) comparison of the mean-square forecast errors from (a) and (b) directly on the same plot.

lead times 5, 15 and 25 days between 60°N and 60°S. As expected, the large values for the ISO signal, and thus large values of the forecast error as well, are predominately confined to the northern tropical latitudes of the eastern hemisphere. At 15 days, the mean signal is still considerably larger than the mean forecast error for this entire region. Not until about the 25-day lead time does the mean forecast error become comparable to the mean signal, indicating potentially useful predictive skill at this lead time. Figure 11 shows the same information as presented in Fig. 10 but for rainfall. As expected, the area exhibiting strong ISO variability is significantly reduced for rainfall as compared to VP200. Apparent is the expected reduction in predictability. For rainfall the error at 15 days lead time is approaching the size of the signal. While 15 days represents about a factor of two reduction relative to the limit of predictability for VP200, taken in the context of typical weather variations it still represents considerable utility, especially if this was in the form of predicting rainfall variations associated with monsoon onsets and breaks.

To show more directly how the signal and error compare versus lead time, predictability ratios defined by Eq. (5) were computed for VP200 and rainfall. Figures 12(a) and (b) show the domain-averaged predictability ratio versus lead time for a rectangular region encompassing most of India, south-east Asia, and Indonesia (i.e. the countries most influenced by the south-east Asian summer monsoon; see larger box in Fig. 11). The ratios are plotted for VP200 and rainfall considering all 168 ISO cases combined. The plots show that on average in this region the predictability ratio remains greater than unity at lead times up until about 25 days for VP200 and 15 days for rainfall. These plots also show the predictability ratios associated with the MJO from an analogous study of NH wintertime (Waliser *et al.* 2003a). Generally, the limits of predictability associated
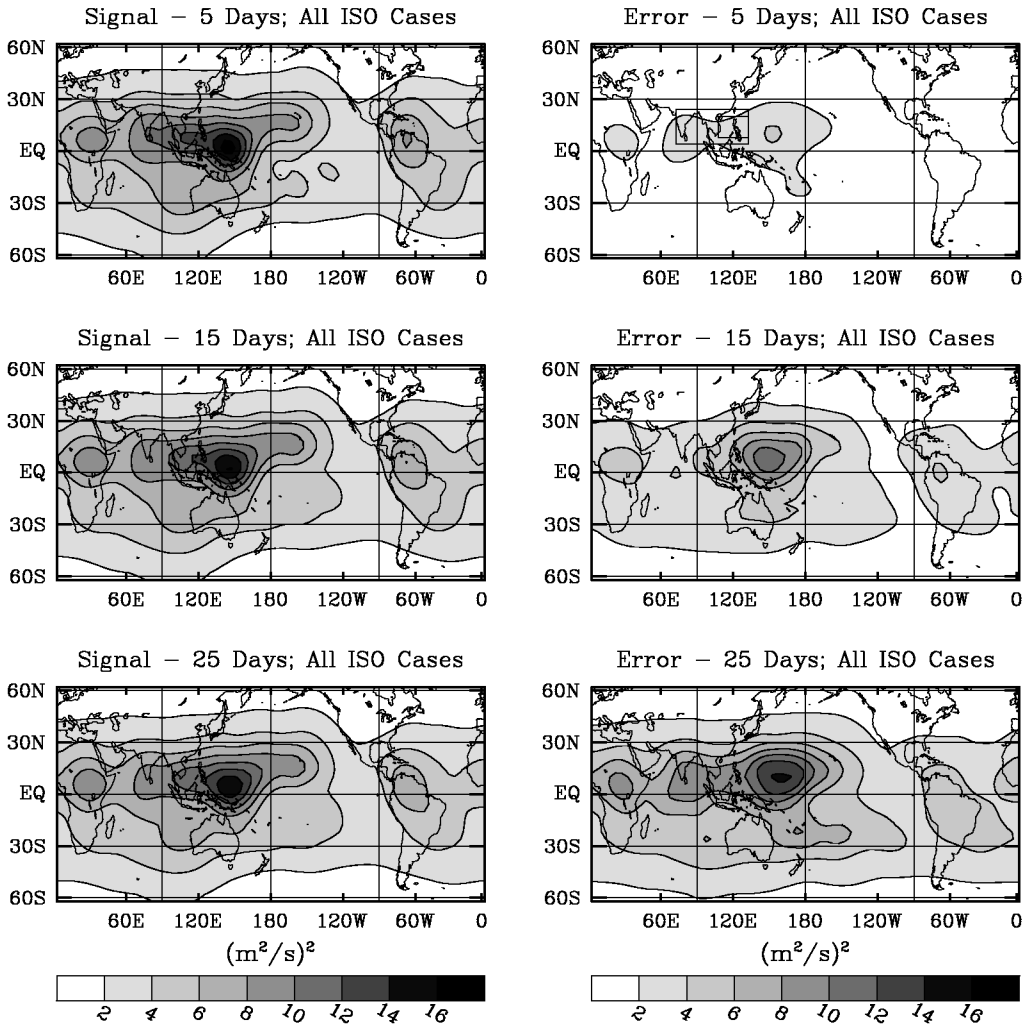
Figure 10.   The intraseasonal oscillation (ISO) mean signal (left-hand side; see Eq. (3)) and mean-square forecast error (right-hand side; see Eq. (4)) for all the selected ISO cases ($N = 168$) at lead times of 5, 15 and 25 days for filtered (30–90 days) 200 hPa velocity potential (VP200). VP200 values have been scaled by 10^{-12}.

with the ISO and MJO for these two quantities appear quite similar, although the MJO appears to exhibit somewhat greater VP200 predictability than the ISO in the 5–15 day range. This overall similarity should not be too surprising given that the two phenomena have very similar time-scales, garner about the same fractions of total variability within their respective seasons, and appear to involve at least somewhat similar dynamical and thermodynamic mechanisms (e.g. Hendon 1988; Jones and Weare 1996; Hendon and Glick 1997; Wang and Xie 1997, 1998; Waliser *et al.* 1999a; Kemball-Cook and Wang 2001; Kemball-Cook and B. Wang 2002; Jones *et al.* 2003). The greater predictability associated with VP200 for the MJO could be associated, at least partly, with the fact that the VP200 variability associated with the model MJO is greater than the model ISO, and its behaviour appears to be more coherent amongst different events (i.e. compare Fig. 7 to Fig. 7 in Waliser *et al.* 2003a). This in turn is likely to be associated with the fact that
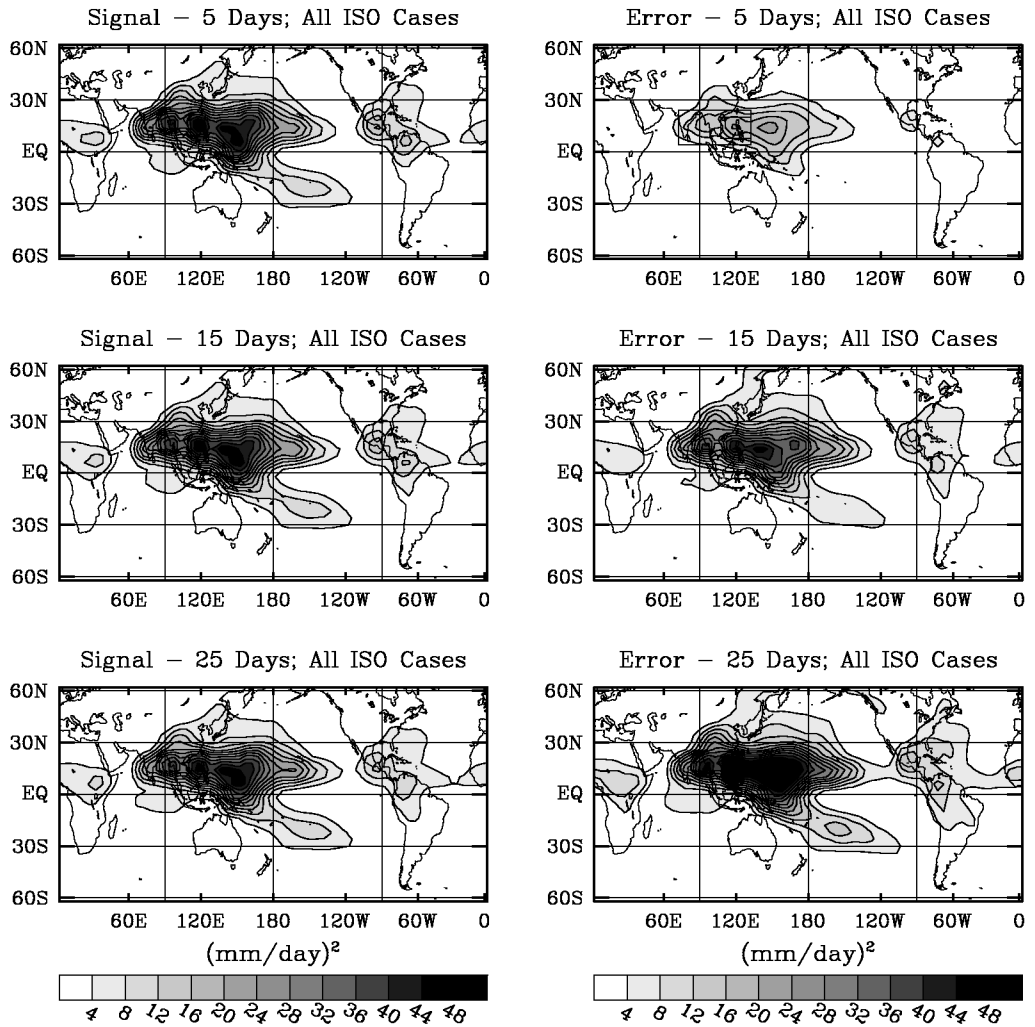
Figure 11.   Same as Fig. 10, except for rainfall.

the (near-equatorial) MJO is more strongly tied to divergent circulation variability than the ISO.

Figures 12(c) and (d) illustrate the difference in predictability ratios over this same region when the forecasts are partitioned into strong versus weak ISO cases. As with Fig. 9, the results show that strong ISO cases exhibit greater predictability than weak ISO cases. Note that over the region considered here, strong events have an average signal (i.e. Eq. (3)) that is about 20% greater than the signal for the weak events. This difference in signal, which is likely to have a bearing on the overall coherence of the ISO events as well as their magnitude, extends the limit of predictability by about 10 days for VP200 and 5 days for rainfall. As discussed above, this sensitivity to ISO strength makes intuitive sense in that as the ISO variability is diminished, the forecasts have less in the way of low-frequency, spatially coherent variability to take advantage of. In particular, at the relatively short time-scales (∼days–weeks) considered here, only high-frequency weather variability remains. To demonstrate the difference
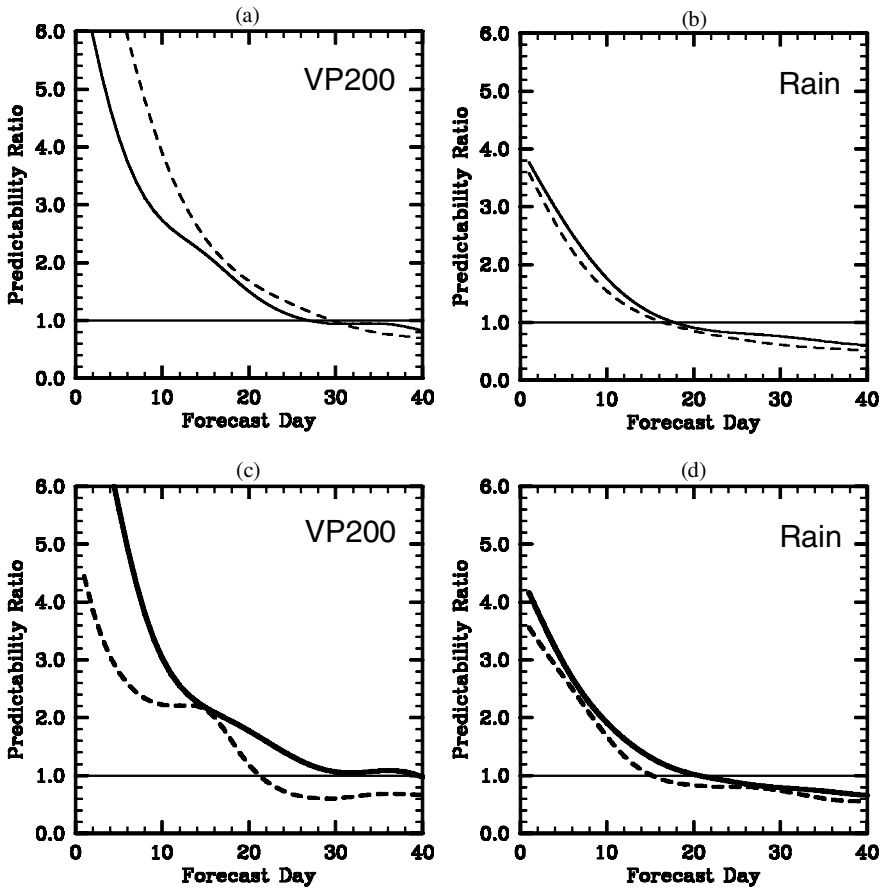
Figure 12. Intraseasonal oscillation (ISO) predictability ratios versus lead time (Eq. (5)) for: (a) 200 hPa velocity potential (VP200), and (b) rainfall averaged over the region 4–24°N, 72.5–132.5°E (see larger box in Fig. 10). The full lines are based on all 168 northern hemisphere (NH) summertime cases from the dynamical forecasts; dashed lines are derived from an analogous set of 120 NH wintertime (i.e. Madden–Julian Oscillation) cases for the region 8°N–16°S, 117.5–167.5°E (see Fig. 12 in Waliser *et al.* 2003a). (b) and (c) are the same as (a) and (b) except that the thick solid (thin dashed) lines are based on forecasts using the strongest (weakest) ISO cases ($N = 80$ in each case; see section 4).

between the model's predictability characteristics for weather over this same region, Fig. 13 compares the predictability ratios for the ISO to that for daily weather variations (see caption for details). In the latter case, unfiltered daily-average data were used from the same region with the value of L in Eq. (1) set to five. Apparent is the considerable and expected reduction in predictability at long leads for the model's weather variations as compared to its ISO variability. In the case of weather, the limit of predictability is about 10 days for both VP200 and rainfall. To illustrate that these limits of predictability are not overly sensitive to the choice of L, Fig. 13 also shows the ISO predictability ratios when L is set to 20, 25, and 30 (i.e. filter lengths of 41, 51 and 61 days) and the weather predictability ratios when L is set to 2, 5 and 8 (i.e. filter lengths of 5, 11 and 17 days). In the ISO case, the change of the filter length by 10 days only influences the estimated limit of predictability by about 1 day. In the weather case, the change of the filter length by 6 days only influences the estimated limit of predictability by about 2 days.
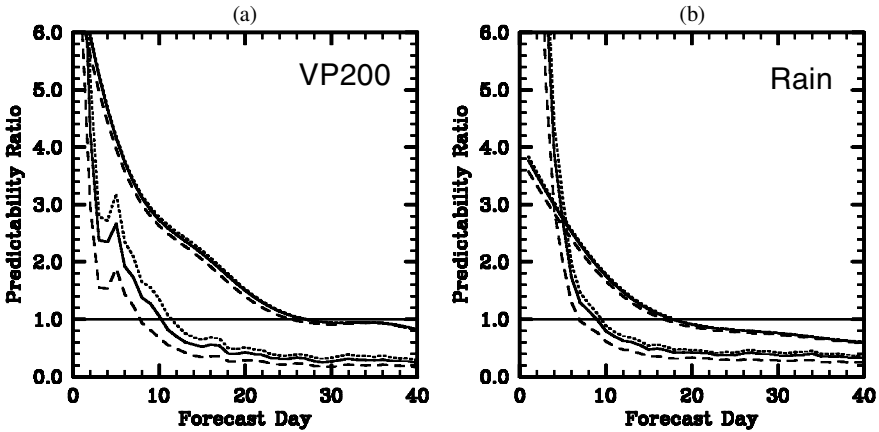
Figure 13. Intraseasonal oscillation (ISO) predictability ratios versus lead time (Eq. (5)) for: (a) 200 hPa velocity potential (VP200), and (b) rainfall, averaged over the region 4–24° N, 72.5–132.5° E (see larger box in Fig. 10). The sets of three lines with greater predictability ratios at long lead times are based on applying Eqs. (1)–(5) to intraseasonally filtered data with L set to 20 (dashed), 25 (solid), and 30 (dotted), where $(2L + 1)$ is the width of the window encompassing a complete ISO event; note that the solid lines from these sets of three lines are the same as the solid lines in the corresponding plots in Figs. 12(a) and (b). The sets of three lines with smaller predictability ratios at long lead times are based on applying Eqs. (1)–(5) to unfiltered data, with L set to 2 (dashed), 5 (solid), and 8 (dotted).

An additional sensitivity test involves examining the dependence of the limit of predictability on the size of the initial perturbation. As discussed in section 3, two different size perturbations were added to the initial conditions to allow at least a cursory examination of this question. When the forecasts are separated into two groups, one for each size perturbation (i.e. $k = 1$ or 2 in Eqs. (1)–(5); $N = 84$), plots such as that in Fig. 13 (not shown) indicate only minor differences. While the set with the larger perturbations (i.e. 0.2 multiplier; see section 3) exhibits a slight reduction in VP200 predictability over the set with smaller perturbations at lead times of about 0–10 days, there is no corresponding systematic difference associated with rainfall, and in each case the limit of predictability is the same. Given the large-scale, low-frequency nature of the ISO, its overall predictability characteristics may not be too sensitive to initial-condition perturbations if they are confined to errors with spatial and temporal scales consistent with weather variations (which was what was attempted here).

Figure 14 compares predictability ratios for forecast associated with each of the four phases of the ISO (see section 3, Figs. 4 and 5). The results show that the predictability is considerably greater, particularly at lead times of 5–15 days, for forecasts that begin when the ISO is in Phase 3, meaning that the area under consideration (see larger box in Figs. 11 and Fig. 5) is convective at the start of the forecast and under suppressed conditions 5–15 later. To more generally examine the sensitivity of the predictability to the sign of the ISO anomaly (i.e. convection or subsidence), the relationship between the VP200 (rainfall) predictability ratios and the mean VP200 (rainfall) anomaly values was examined. To do so, mean band-passed VP200 and rainfall anomaly values over a given set (i.e. Phase 1, 2, 3 or 4) of ISO cases were computed as follows:

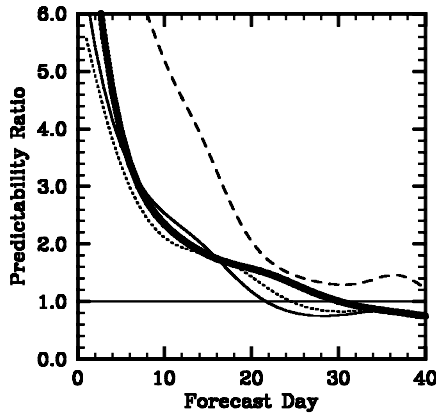$$\overline{X_j^0} = \frac{1}{N} \sum_{i=1}^{N} X_{ij}^0, \qquad (6)$$

Figure 14. Intraseasonal oscillation (ISO) predictability ratios versus lead time (Eq. (5)) for 200 hPa velocity potential (VP200) averaged over the region 4–24°N, 72.5–132.5°E (see larger box in Fig. 10). Each different line is associated with ISO cases from only one of the four ISO phases (see Figs. 4 and 5), thus each is based on 42 forecasts (i.e. 21 cases of 2 perturbations): Phase 1, thin solid; Phase (2), dotted; Phase 3, dashed; and Phase 4, thick solid.

where i represents the case index and N is 21. Note that this computation is tantamount to constructing the thick solid line shown in Fig. 7 for each grid point. These mean band-passed anomalies (Eq. (6)) as well as the mean predictability ratios (Eq. (5)) each have latitude, longitude, forecast day and ISO phase dependence. Figures 15(a) and (b) show the VP200 and rainfall predictability ratios, bin-averaged against the band-passed VP200 and rainfall anomalies, respectively, and lead time from a large domain that exhibits relatively strong NH summertime intraseasonal variability. In this case, the latitude, longitude and ISO phase (i.e. Phase 1–4) dependencies were averaged out to leave only the dependence of predictability on lead time and mean anomaly value. Figures 15(c) and (d) indicate the 95% significance levels of the above relationships at lead times of 15 days. The results from this analysis show that the predictability values, as defined in Eq. (5), tend to be slightly greater at longer lead times for the suppressed phase of the oscillation. At short lead times ($\lesssim 5$ days), significantly greater model predictability for rainfall tends to be biased towards the convective phase of the ISO (not shown), with no significant relationship found at short leads for VP200. These results are consistent with what was illustrated in Fig. 14 and largely consistent with the results found for the MJO in (Waliser *et al.* 2003a). The only difference between the present results shown in Fig. 15 and the results from the analogous analysis of the MJO (their Fig. 13) is that VP200 also tended to exhibit higher predictability at short leads (i.e. 3 days) under convective (i.e. negative VP200) anomalies, although the relationship was weak compared to that for rainfall. Thus the aspects that are consistent between both these studies are that convective conditions, in terms of rainfall, appear to be more predictable at very short leads (~ 3 days), and suppressed conditions, in terms of rainfall and VP200, appear to be more predictable at long leads (~ 15 days).

Finally, to examine the dependency of the predictability values discussed above on the modal characteristics of the model's intraseasonal variability and to demonstrate that the enhanced predictability at long lead times is in fact derived from the model's ISO, mean-square forecast errors were calculated for model EOF amplitude series. To do so, the filtered summertime (May–October) band-passed VP200 data from the control simulation were subject to a standard EOF analysis. The spatial structures of the first
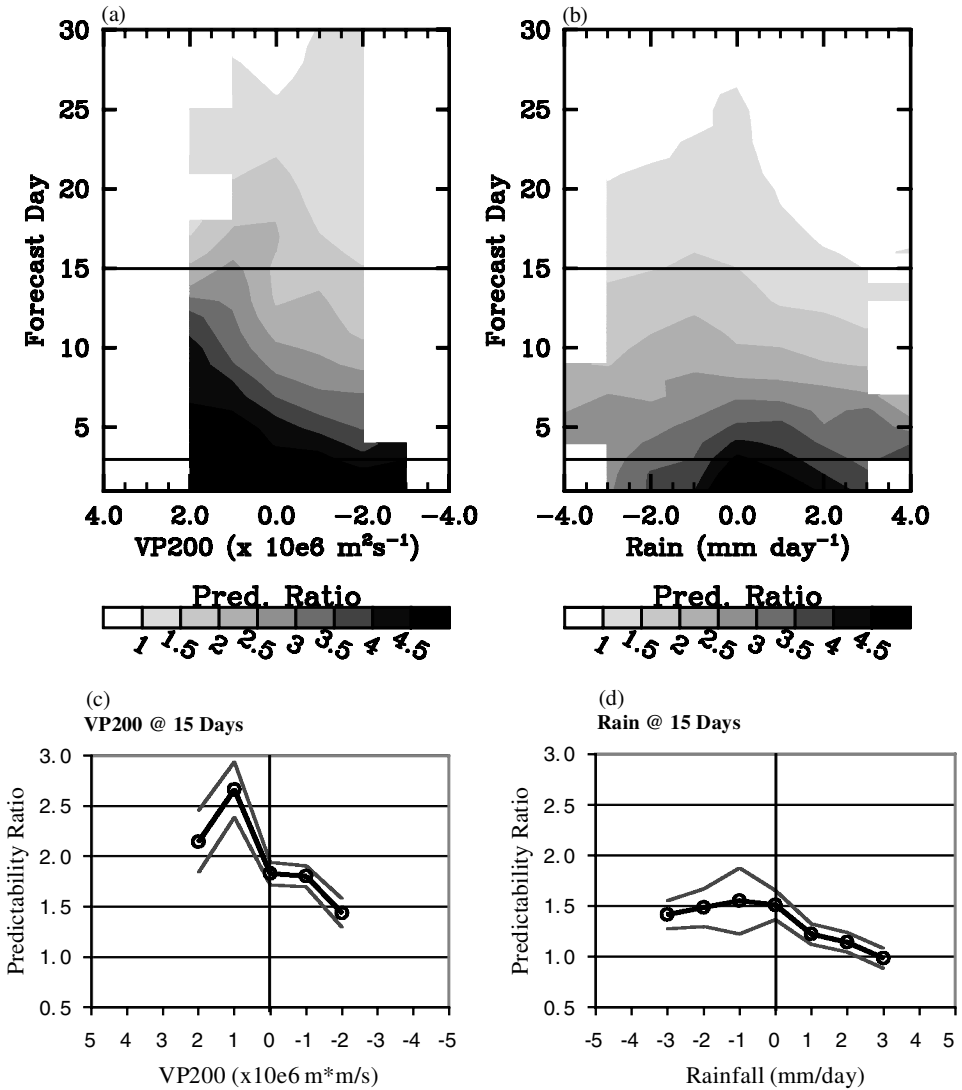
Figure 15. (a) Mean predictability ratios (Eq. (5)) for 200 hPa velocity potential (VP200) versus lead time (vertical axis) and mean filtered VP200 anomaly value (horizontal axis); (b) as (a) but for rainfall. Predictability ratios and anomalies were taken from model grid points in the region 4–24°N and 62.5°E–147.5°W. Only bins with number of cases $N > 20$ are plotted. (c) Predictability ratios of VP200 (thick lines) at forecast day 15 (see upper horizontal line on (a) and (b)), with 95% confidence intervals on the means using a Students t-test (thin lines); (d) as (c) but for rainfall.

two EOF vectors resemble the second and third model composite VP200 panels shown in Fig. 3. EOF amplitude time series were computed using this modal structure for the control and perturbed forecasts for all the selected ISO cases. These amplitude time series, which are unit normalized, were then used in place of the actual data in Eqs. (1), (2) and (4) to compute the mean-square forecast error for each EOF mode. In this case, the forecasts for all four ISO phases and both perturbation sizes were considered together. Figures 16(a) and (b) show these EOF amplitude forecast errors versus lead time, partitioned into results for the strong and weak ISO cases, respectively

(a) **Strong ISO Cases**

(b) **Weak ISO Cases**
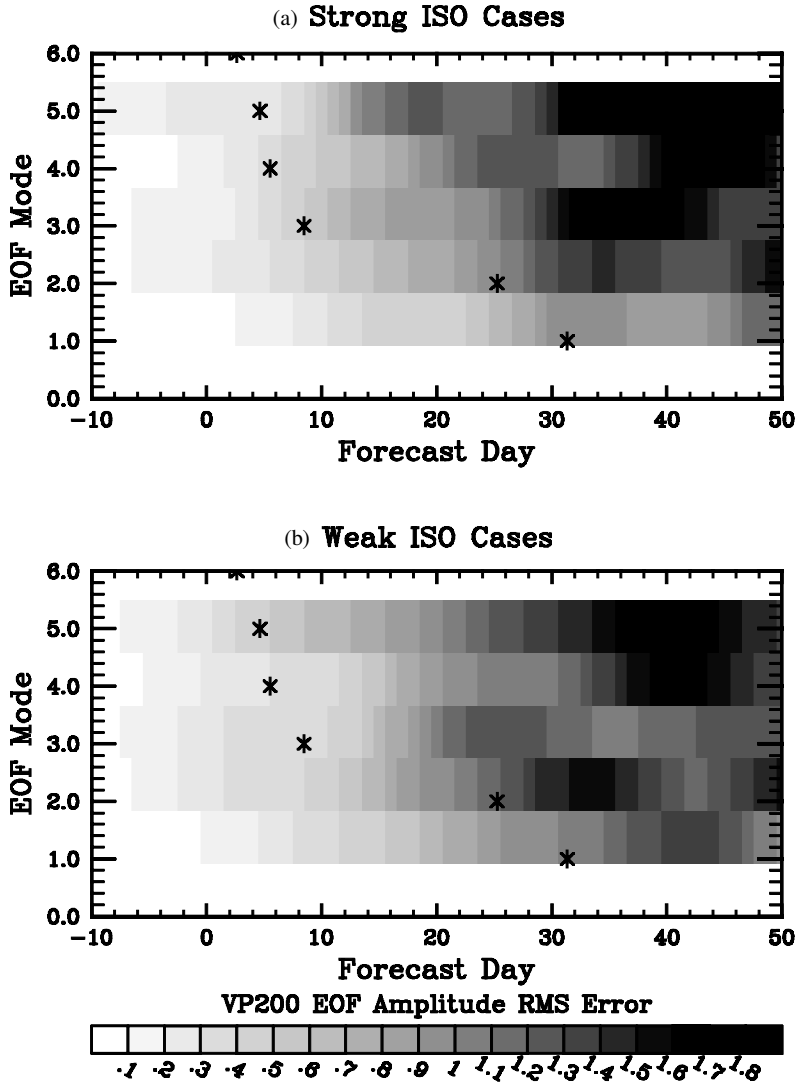

VP200 EOF Amplitude RMS Error

Figure 16.   (a) Mean RMS forecast errors (Eq. (4)) versus forecast day of the empirical orthogonal function (EOF) time series (modes 1–5) of 200 hPa velocity potential for the strongest ten selected intraseasonal oscillation (ISO) cases combined; (b) as (a) but for the weakest ten ISO cases. Star symbols indicate the percentage variance associated with each EOF mode using the same x-axis interpreted as percentage (%).

(see discussion associated with Fig. 9 for what constitutes the strong and weak cases). The stars shown on Fig. 16 are the variance percentages associated with the VP200 summertime EOF modes.

The results associated with the strong ISO cases demonstrate that the model forecast errors associated with the lowest two EOF modes, those that capture most of the ISO variability, tend to be considerably lower at most lead times than the forecast errors for the higher order modes. In fact their forecast errors at lead times of 20 days are comparable to the forecast errors of the higher order modes at 10–15 days. Keep in mind that, given the significantly greater variance of the first two modes (∼56% of the

band-passed variance), most of the overall error is still coming from these two modes. However, as in most forecasting settings, errors associated with the higher order modes are likely to be influencing the development of errors of the lower order modes. For the weaker ISO cases the above relationship is still generally true, particularly in regards to the lowest order mode, however the growth rate of errors for modes 1 and 2 is relatively higher than for the strong ISO cases, while the opposite is true for the higher order modes. These results are consistent with the fact that for the strong ISO cases, more energy is organized (i.e. they have high EOF/EEOF amplitudes) into the low-frequency variations of the ISO modal structure that inherently stays coherent for longer periods. Even in the face of significant error growth of the higher order modes, the impact of this is relatively small since they encompass so much less of the overall variance ($\sim$5%). On the other hand, for the weaker ISO cases the relative imbalance between the variances in the low order ISO modes and that in the higher order modes is less (i.e. they have smaller EOF/EEOF amplitudes than for the strong case; not shown). In this case, it is likely that the energy in the higher order modes can lead to a quicker deterioration of the coherent, but in these cases weaker, ISO modes.

5. CONCLUSIONS

The goal of this study is to provide an initial estimate of the dynamic predictability of the tropical ISO that is associated with the south-east Asian monsoon. The NASA GLA general circulation model was chosen for this study due to its relatively realistic ISO representation (Fig. 3, section 2). A 10-year control simulation using specified annual cycle SSTs was performed in order to provide initial conditions from which to perform an ensemble of twin predictability experiments. The initial conditions were taken from periods of strong ISO activity identified via extended EOF analysis of 30–90 day band-passed tropical rainfall (Figs. 2 and 4). From this analysis, 21 cases were chosen when the ISO convection anomaly was associated with four distinct ISO phases (Figs. 3–5), making 84 cases in total. Two different sets of small random perturbations were added to these 84 initial states. Simulations were then performed for 90 days from each of these 168 perturbed initial conditions.

A measure of potential predictability was constructed based on a ratio of the signal associated with the ISO, in terms of rainfall or 200 hPa velocity potential (VP200), and the mean-square error between sets of twin forecasts (defined in Eqs. (1)–(5); Figs. 8–12). The limit of predictability was considered to extend through lead times for which this ratio remained less than one, and thus during the period when the mean-square error was less than the signal associated with the ISO. The results indicate that the limit of predictability for this model's ISO extends out to about 25 days for VP200 and to about 15 days for rainfall (Figs. 10–12). This limit is comparable to the limit suggested by empirical methods of ISO prediction based on the model data (Fig. 8) or on observational data (Waliser *et al.* 1999b). While this latter comparison provides some reassuring support for the dynamical estimates of ISO predictability, it also bolsters some confidence in AGCMs, in a manner suggesting that we may be approaching the point (or at least in the not too distant future) when ISO prediction may become a practical and useful endeavour.

The predictability measure shows sensitivity to the strength of the ISO (Fig. 12), in that the limit of predictability for the subset of strong ISO cases extends about 10 (5) days longer for VP200 (rainfall) than for a subset of weak ISO cases, the latter of which had an average signal about 20% smaller than the former. As discussed earlier, this is not surprising since as the ISO variability weakens, the only remaining variability

at time-scales of order days to weeks is associated with tropical weather, which is inherently less predictable (Fig. 13). The predictability measure also shows modest dependence on the phase of the ISO, with greater predictability for the convective phase at short ($\lesssim 5$ days) lead times and for the suppressed phase at longer ($\gtrsim 10$ days) lead times (Figs. 14 and 15). The reason for this dependence is not obvious. At short lead times, if the model atmosphere has built up sufficient vertical instability on a large-scale, convection may be nearly ensured making the predictability higher. While in regions where convection is expected to be suppressed, the model may simply have a tendency towards convection making predictability at shorter lead times more difficult relative to convective regions. At longer lead times, pin-pointing the place and time of convection may simply be more difficult than predicting what would typically be a larger-scale region of subsidence. Mean-square forecast errors were also computed for EOF amplitude time series of the band-passed model output (Fig. 14) to highlight the fact that the enhanced predictability at extended range is derived mostly from the first two modes, i.e. those that capture the model's representation of the ISO. For the most part, the results and predictability characteristics summarized above are consistent with those found by a companion study for NH wintertime tropical intraseasonal variability (i.e. MJO, Waliser *et al.* 2003a).

These results have important implications for both the local regions that the ISO rainfall variations impact directly (e.g. monsoons of India and south-east Asia) as well as regions that are influenced by the ISO via teleconnections. Present day atmospheric forecasts are largely directed toward predicting short-term weather variations from analysed initial conditions as well as seasonal climate variations associated with seasonal/interannual changes in surface boundary conditions, namely from tropical SSTs. As yet, operational weather forecasts have largely been unable to exploit the relatively strong signal and slow evolution associated with the ISO (e.g. Waliser *et al.* 1999b; Hendon *et al.* 2000; Jones *et al.* 2000). This is due to the generally poor representation of the ISO in most AGCMs, except for a few research-oriented models (e.g. Slingo *et al.* 1996; Waliser *et al.* 1999b; Waliser and Hogan 2000; Waliser *et al.* 2003b). However, if the ISO could be better represented in operational weather forecast models, particularly in terms of stronger amplitudes and more coherent structures, the above results imply that extended-range tropical forecasts in the regions directly impacted by the ISO (e.g. Fig. 3) could be greatly enhanced and/or extended. This certainly includes a means to better predict the onset and break periods of the Asian–Australian summer monsoons. In addition, it might also lead to improvements in predicting some aspects of midlatitude weather variability (e.g. summertime rainfall over Mexico, Pacific–South America circulation, hurricane development).

There are a number of caveats that should be noted regarding the above results. For example, there are model shortcomings that suggest the above results might be an underestimate of predictability of the ISO. First, while the intraseasonal peaks of equatorial wave-number one, upper-level velocity potential and zonal wind for the model are quite similar, in terms of magnitude and frequency, to observations, the model spectra have too much high-frequency ($\sim$days) variability (Slingo *et al.* 1996). This result is primarily based on analysis of NH wintertime ISO (i.e. MJO) variability but is still likely to have bearing on the summertime counterpart (Waliser *et al.* 2003b). Relative to the ISO, this high-frequency variability would be considered to be disorganized, errant convective activity that may erode the relatively smooth evolution of the ISO and thus possibly diminish its predictability. Second, these simulations were carried out with fixed climatological SST values. A previous study with this model showed that coupled SSTs tend to have an enhancing and organizing influence on the model ISO (Waliser

et al. 1999a), making it stronger and more coherent (cf. Flatau *et al.* 1997; Kemball-Cook and Wang 2002). Thus the exclusion of SST coupling may lead to an underestimate of the predictability as well. The third aspect that may lead to an underestimate of the predictability is the fact that the model contains too little variability over the equatorial Indian Ocean (Fig. 3). The weakened ISO rainfall variations over this region may lead to reduced predictability due to the model's relatively weak convection passing through this region, a region that exhibits a relatively robust convective signal in the observations.

A number of aspects associated with the model and/or analysis suggest that the above results might overestimate the predictability of the ISO. The first is that the model's coarse resolution and inherent reduced degrees of freedom relative to the true atmosphere may limit the amount of small-scale variability that would typically erode large time- and space-scale variability. However, it is important to note in this regard that the low order EOFs of intraseasonally filtered model output typically do not capture as much variability as analogous EOFs of observed quantities (section 3). Thus, while it may be true that the model lacks sufficient small-scale variability which may erode ISO predictability, the model's ISO itself, as indicated above, still has room to be more robust and coherent which would tend to enhance predictability. In addition to model shortcomings, the simple manner that perturbations were added to the initial conditions may also lead to an overestimate of the predictability. The perturbation structure and the size of the perturbations (see section 3) may be too conservative and not adequately represent the type of initial-condition error that would be found in an operational context. However, even if that is the case, it would seem that 'initial' errors of adequate size would occur in the forecast in a matter of a day or two, and thus one would expect this aspect to overestimate the predictability by only a couple days, if at all.

In regard to the above results and conclusions, we would like to stress that the limit of predictability for the ISO reported here is purely theoretical, based on relatively strong ISO events as simulated in a single AGCM. The analysis and its intent were to ascertain the limit of predictability of ISO events themselves. However, it should be noted the overall predictability of tropical variability on intraseasonal time-scales is bound to be less on average, since periods in between ISO events would generally only be composed of 'weather' variability and thus be less predictable. Moreover, it is wholly acknowledged that the AGCM employed here contains shortcomings regarding its representation of intraseasonal variability that may certainly influence this study's estimate of ISO predictability. Future studies will examine the sensitivity of these results to the AGCM employed, SST coupling, midlatitude variability, and El Niño state, as well as examine how sensitive these results are to the initial condition perturbations and definition of predictability.

REFERENCES

Anderson, J. L. and Stern, W. F.	1996	Evaluating the potential predictive utility of ensemble forecasts. *J. Climate*, **9,** 260–269
Arakawa, A. and Lamb, V. R.	1977	Computational design of the basic dynamical processes of the UCLA general circulation model. Pp. 173–265 in *Methods in computational physics*. Ed. Chang. Academic Press, New York, USA
Arakawa, A. and Schubert, W. H.	1974	Interaction of a cumulus cloud ensemble with large-scale environment: 1. *J. Atmos. Sci.*, **31,** 674–701
Banerjee, A. K., Sen, P. N. and Raman, C. R. V.	1978	On foreshadowing southwest monsoon rainfall over India with mid-tropospheric circulation anomaly of April. *Indian J. Meteorol. Hydrol. Geophys.*, **29,** 425–431
Banerji, S. K.	1950	Methods of foreshadowing monsoon and winter rainfall in India. *Indian J. Meteorol. Geophys.*, **1,** 4–14
Bansod, S. D., Singh, S. V. and Kripalani, R. H.	1991	The relationship of monsoon onset with subsequent rainfall over India. *Int. J. Climatol.*, **11,** 809–817
Barnston, A. G., Glantz, M. H. and He, Y. X.	1999	Predictive skill of statistical and dynamical climate models in SST forecasts during the 1997–98 El Niño episode and the 1998 La Nina onset. *Bull. Am. Meteorol. Soc.*, **80,** 217–243
Blanford, H. F.	1884	On the connection of the Himalayan snowfall with dry winds and seasons of droughts in India. *Proc. R. Soc. London*, **37,** 3
Cadet, D. L.	1986	Fluctuations of precipitable water over the Indian Ocean during the 1979 summer monsoon. *Tellus Ser. A-Dyn. Meteorol. Oceanol.*, **38,** 170–177
Cane, M. A., Zebiak, S. E. and Dolan, S. C.	1986	Experimental forecasts of El-Niño. *Nature*, **321,** 827–832
Charney, J., Fleagle, R. G., Lally, V. E., Riehl, H. and Wark, D. Q.	1966	The feasibility of a global observation and analysis experiment. *Bull. Am. Meteorol. Soc.*, **47,** 200–220
DelSole, T. and Shukla, J.	2002	Linear prediction of Indian monsoon rainfall. *J. Climate*, **15,** 3645–3658
Duchon, C. E.	1979	Lanczos filter in one and two dimensions. *J. Appl. Meteorol.*, **18,** 1016–1022
Fennessy, M. J., Kinter, J. L., Kirtman, B., Marx, L., Nigam, S., Schneider, E., Shukla, J., Straus, D., Vernekar, A., Xue, Y. and Zhou, J.	1994	The simulated Indian monsoon—a GCM sensitivity study. *J. Climate*, **7,** 33–43
Flatau, M., Flatau, P. J., Phoebus, P. and Niller, P. P.	1997	The feedback between equatorial convection and local radiative and evaporative processes: The implications for intraseasonal oscillations. *J. Atmos. Sci.*, **54,** 2373–2386
Gates, W. L. and Nelson, A. B.	1975	'A new (revised) tabulation of the Scripps topography on a one-degree global grid. Part 1: Terrain heights'. Tech. Report R-1276-1-ARPA, The Rand Corporation, Santa Monica, CA, USA
Graham, N. E. and Barnett, T. P.	1995	ENSO and ENSO-related predictability. 2. Northern hemisphere 700 mb height predictions based on a hybrid coupled ENSO model. *J. Climate*, **8,** 544–549
Guhathakurta, P., Rajeevan, M. and Thapliyal, V.	1999	Long range forecasting Indian summer monsoon rainfall by a hybrid principal component neural network model. *Meteorol. Atmos. Phys.*, **71,** 255–266
Harshvardhan, R., Davies, D., Randall, A. and Corsetti, T. G.	1987	A fast radiation parameterization for general circulation models. *J. Geophys. Res.*, **92,** 1009–1026
Hastenrath, S.	1987	On the prediction of India monsoon rainfall anomalies. *J. Clim. Appl. Meteorol.*, **26,** 847–857
	1995	Recent advances in tropical climate prediction. *J. Climate*, **8,** 1519–1532
Hastenrath, S. and Greischar, L.	1993	Changing predictability of Indian monsoon rainfall anomalies. *Proc. Indian Acad. Sci.-Earth Planet. Sci.*, **102,** 35–47
Helfand, H. M. and Labraga, J. C.	1988	Design of a non-singular level 2.5 second order closure model for prediction of atmospheric turbulence. *J. Atmos. Sci.*, **45,** 113–132
Hendon, H. H.	1988	A simple-model of the 40–50 day oscillation. *J. Atmos. Sci.*, **45,** 569–584

Hendon, H. H. and Glick, J.	1997	Intraseasonal air–sea interaction in the tropical Indian and Pacific Oceans. *J. Climate*, **10,** 647–661
Hendon, H. H., Liebmann, B., Newman, M., Glick, J. D. and Schemm, J. E.	2000	Medium-range forecast errors associated with active episodes of the Madden–Julian oscillation. *Mon. Weather Rev.*, **128,** 69–86
Higgins, R. W. and Shi, W.	2001	Intercomparison of the principal modes of interannual and intraseasonal variability of the North American monsoon system. *J. Climate*, **14,** 403–417
Jagannathan, P.	1960	'Seasonal forecasting in India, a review'. Meteorological Office, Poona, India
Jones, C. and Weare, B. C.	1996	The role of low-level moisture convergence and ocean latent heat fluxes in the Madden and Julian oscillation: An observational analysis using ISCCB data and ECMWF analyses. *J. Climate*, **9,** 3086–3104
Jones, C., Waliser, D. E., Schemm, J.-K. E. and Lau, W. K. M.	2000	Prediction skill of the Madden and Julian Oscillation in dynamical extended range forecasts. *Clim. Dyn.*, **16,** 273–289
Jones, C., Carvalho, L. M. V., Higgins, R. W., Waliser, D. E. and Schemm, J.-K. E.	2003	Climatology of tropical intraseasonal convective anomalies 1979–2002. *J. Climate*, in press
Kalnay, E. R., Balgovind, W., Chao, D., Edelmann, J., Pfaendtner, L., Takacs, and Takano, K.	1983	'Documentation of the GLAS fourth order general circulation model, Volume 1'. NASA Tech. Memo. No. 86064, NASA Goddard Space Flight Center, Greenbelt, MD, USA
Kang, I. S., Jin, K., Lau, K., M. Shukla, J., Krishnamurthy, V., Schubert, S. D., Waliser, D. E., Stern, W. F., Satyan, V., Kitoh, A., Meehl, G. A., Kanamitsu, M., Galin, V. Y., Kim, J. K., Sumi, A., Wu, G. and Liu, Y.	2002a	Intercomparison of GCM simulated anomalies associated with the 1997–98 El Niño. *J. Climate*, **15,** 2791–2805
Kang, I. S., Jin, K., Wang, B., Lau, K. M., Shukla, J., Schubert, S. D., Waliser, D. E., Krishnamurthy, V., Stern, W. F., Satyan, V., Kitoh, A., Meehl, G. A., Kanamitsu, M., Galin, V. Y., Kim, J. K., Sumi, A., Wu, G. and Liu, Y.	2002b	Intercomparison of the climatological variations of Asian summer monsoon precipitation simulated by 10 GCMs. *Clim. Dyn.*, **19,** 383–395
Kemball-Cook, S. and Wang, B.	2001	Equatorial waves and air–sea interaction in the Boreal summer intraseasonal oscillation. *J. Climate*, **14,** 2923–2942
Kemball-Cook, S., Wang, B. and Fu, X.	2002	Simulation of the ISO in the ECHAM4 model: The impact of coupling with an ocean model. *J. Atmos. Sci.*, **59,** 1433–1453
Kershaw, R.	1988	The effect of a sea-surface temperature anomaly on a prediction of the onset of the south-west monsoon over India. *Q. J. R. Meteorol. Soc.*, **114,** 325–345
Kirtman, B. P., Shukla, J., Huang, B. H., Zhu, Z. X. and Schneider, E. K.	1997	Multiseasonal predictions with a coupled tropical ocean–global atmosphere system. *Mon. Weather Rev.*, **125,** 789–808
Krishna Kumar, K., Soman, M. K. and Rupa Kumar, K.	1995	Seasonal forecasting of Indian summer monsoon rainfall. *Weather*, **50,** 449–467
Krishnamurti, T. N., Subramaniam, M., Oosterhof, D. K. and Daughenbaugh, G.	1990	Predictability of low-frequency modes. *Meteorol. Atmos. Phys.*, **44,** 63–83
Krishnamurti, T. N., Subramaniam, M., Daughenbaugh, G., Oosterhof, D. and Xue, J. H.	1992	One-month forecasts of wet and dry spells of the monsoon. *Mon. Weather Rev.*, **120,** 1191–1223
Kumar, K. K., Rajagopalan, B. and Cane, M. A.	1999	On the weakening relationship between the Indian monsoon and ENSO. *Science*, **284,** 2156–2159
Kung, E. C. and Sharif, T. A.	1980	Regression forecasting of the onset of the Indian summer monsoon with antecedent upper air conditions. *J. Appl. Meteorol.*, **19,** 370–380

| Kung, E. C. and Sharif, T. A. | 1982 | Long-range forecasting of the Indian summer monsoon onset and rainfall with upper air parameters and sea-surface temperature. *J. Meteorol. Soc. Jpn.*, **60,** 672–681 |

Lau, K. M. and Chan, P. H. 1986 Aspects of the 40–50 day oscillation during the northern summer as inferred from outgoing longwave radiation. *Mon. Weather Rev.*, **114,** 1354–1367

Lo, F. and Hendon, H. H. 2000 Empirical extended-range prediction of the Madden–Julian oscillation. *Mon. Weather Rev.*, **128,** 2528–2543

Lord, S. J. and Arakawa, A. 1980 Interaction of a cumulus cloud ensemble with the large-scale environment. 2. *J. Atmos. Sci.*, **37,** 2677–2692

Lorenz, E. N. 1965 A study of the predictability of a 28-variable atmospheric model. *Tellus*, **17,** 321–333

1982 Atmospheric predictability experiments with a large numerical model. *Tellus*, **34,** 505–513

Madden, R. A. and Julian, P. R. 1994 Observations of the 40–50-day tropical oscillation—a review. *Mon. Weather Rev.*, **122,** 814–837

Maloney, E. D. and Hartmann, D. L. 2000a Modulation of eastern North Pacific hurricanes by the Madden–Julian oscillation. *J. Climate*, **13,** 1451–1460

2000b Modulation of hurricane activity in the Gulf of Mexico by the Madden–Julian oscillation. *Science*, **287,** 2002–2004

Mo, K. C. 2000a The association between intraseasonal oscillations and tropical storms in the Atlantic basin. *Mon. Weather Rev.*, **128,** 4097–4107

2000b Intraseasonal modulation of summer precipitation over North America. *Mon. Weather Rev.*, **128,** 1490–1505

2001 Adaptive filtering and prediction of intraseasonal oscillations. *Mon. Weather Rev.*, **129,** 802–817

Mo, K. C. and Higgins, R. W. 1998 The Pacific–South American modes and tropical convection during the southern hemisphere winter. *Mon. Weather Rev.*, **126,** 1581–1596

Mooley, D. A., Parthasarathy, B. and Pant, G. B. 1986 Relationship between Indian summer monsoon rainfall and location of the ridge at the 500 mb level along 75 degrees E. *J. Clim. Appl. Meteorol.*, **25,** 633–640

Normand, C. W. B. 1953 Monsoon seasonal forecasting. *Q. J. R. Meteorol. Soc.*, **79,** 463–473

Palmer, T. N. 1993 Extended-range atmospheric prediction and the Lorenz model. *Bull. Am. Meteorol. Soc.*, **74,** 49–65

Parthasarathy, B., Kumar, K. R. and Deshpande, V. R. 1991 Indian summer monsoon rainfall and 200 mb meridional wind index—application for long-range prediction. *Int. J. Climatol.*, **11,** 165–176

Parthasarathy, B., Kumar, K. R. and Munot, A. A. 1993 Homogeneous Indian monsoon rainfall—variability and prediction. *Proc. Indian Acad. Sci.-Earth Planet Sci.*, **102,** 121–155

Pasch, R. J. 1981 Numerical prediction of the onset of the planetary scale monsoon. *Bull. Am. Meteorol. Soc.*, **62,** 903–903

Phillips, T. J. 1994 'A summary documentation of the AMIP models'. Report 18 PCMDI, Lawrence Livermore National Laboratory, California, USA

Prasad, K. D. and Singh, S. V. 1992 Possibility of predicting Indian monsoon rainfall on reduced spatial and temporal scales. *J. Climate*, **5,** 1357–1361

1996 Forecasting the spatial variability of the Indian monsoon rainfall using canonical correlation. *Int. J. Climatol.*, **16,** 1379–1390

Rajeevan, M., Pai, D. S. and Thapliyal, V. 1998 Spatial and temporal relationships between global land surface air temperature anomalies and Indian summer monsoon rainfall. *Meteorol. Atmos. Phys.*, **66,** 157–171

Sahai, A. K., Soman, M. K. and Satyan, V. 2000 All India summer monsoon rainfall prediction using an artificial neural network. *Clim. Dyn.*, **16,** 291–302

Schemm, J. E. 1997 'Application of dynamic extended range forecasts to the prediction of the Asian monsoon'. In Proceedings of the third international study conference on GEWEX in Asia and GAME, Cheju, Korea

Schneider, T. and Griffies, S. M. 1999 A conceptual framework for predictability studies. *J. Climate*, **12,** 3133–3155

Sellers, P. J., Mintz, Y., Sud, Y. C. and Dalcher, A. 1986 A simple biosphere model (SiB) for use within general circulation models. *J. Atmos. Sci.*, **43,** 505–531

Shapiro, R. 1970 Smoothing, filtering and boundary effects. *Rev. Geophys. Space Phys.*, **8,** 359–387

Shukla, J. 1985a Prospects for dynamical long-range prediction of monsoons. *Curr. Sci.*, **54**, 327–329

1985b Predictability. *Adv. Geophys.*, **28B**, 87–122

Shukla, J. and Mooley, D. A. 1987 Empirical prediction of the summer monsoon rainfall over India. *Mon. Weather Rev.*, **115**, 695–703

Shukla, J. and Paolino, D. A. 1983 The southern oscillation and long-range forecasting of the summer monsoon rainfall over India. *Mon. Weather Rev.*, **111**, 1830–1837

Slingo, J. M., Sperber, K. R., Boyle, J. S., Ceron, J. P., Dix, M., Dugas, B., Ebisuzaki, W., Fyfe, J., Gregory, D., Gueremy, J. F., Hack, J., Harzallah, A., Inness, P, Kitoh, A., Lau, W. K. M., McAvaney, B., Madden, R., Matthews, A., Palmer, T. N., Park, C. K., Randall, D. and Renno, N. 1996 Intraseasonal oscillations in 15 atmospheric general circulation models: Results from an AMIP diagnostic subproject. *Clim. Dyn.*, **12**, 325–357

Sperber, K. R. and Palmer, T. N. 1996 Interannual tropical rainfall variability in general circulation model simulations associated with the atmospheric model intercomparison project. *J. Climate*, **9**, 2727–2750

Sperber, K. R., Slingo, J. M., Inness, P. M. and Lau, W. K. M. 1997 On the maintenance and initiation of the intraseasonal oscillation in the NCEP/NCAR reanalysis and in the GLA and UKMO AMIP simulations. *Clim. Dyn.*, **13**, 769–795

Sperber, K. R., Slingo, J. M. and Annamalai, H. 2000 Predictability and the relationship between subseasonal and interannual variability during the Asian summer monsoon. *Q. J. R. Meteorol. Soc.*, **126**, 2545–2574

Sperber, K. R., Brankovic, C., Deque, M., Frederiksen, C. S., Graham, R., Kitoh, A., Kobayashi, C., Palmer, T., Puri, K., Tennant, W. and Volodin, E. 2001 Dynamical seasonal predictability of the Asian summer monsoon. *Mon. Weather Rev.*, **129**, 2226–2248

Stern, W. and Miyakoda, K. 1995 Feasibility of seasonal forecasts inferred from multiple GCM simulations. *J. Climate*, **8**, 1071–1085

Sud, Y. C. and Walker, G. K. 1992 A review of recent research on improvement of physical parameterizations in the GLA GCM. Pp. 422–479 in *Physical processes in atmospheric models*. Eds. D. R. S. and S. S. Singh. Wiley Eastern Ltd., New Delhi, India

Thapliyal, V. and Kulshrestha, S. M. 1992 Recent models for long-range forecasting of southwest monsoon rainfall in India. *Mausum*, **43**, 239–248

Thompson, P. D. 1957 Uncertainty of initial state as a factor in the predictability of large scale atmospheric flow patterns. *Tellus*, **9**, 275–295

van den Dool, H. M. 1994 Long-range weather forecasts through numerical and empirical methods. *Dyn. Atmos. Ocean*, **20**, 247–270

Waliser, D. E. and Hogan, T. F. 2000 Analysis of ocean surface heat fluxes in a NOGAPS climate simulation: Influences from convection, clouds and dynamical processes. *J. Geophys. Res.-Atmos.*, **105**, 4587–4606

Waliser, D. E., Lau, K. M. and Kim, J. H. 1999a The influence of coupled sea surface temperatures on the Madden–Julian oscillation: A model perturbation experiment. *J. Atmos. Sci.*, **56**, 333–358

Waliser, D. E., Jones, C., Schemm, J. K. E. and Graham, N. E. 1999b A statistical extended-range tropical forecast model based on the slow evolution of the Madden–Julian oscillation. *J. Climate*, **12**, 1918–1939

Waliser, D. E., Lau, K. M., Stern, W. and Jones, C. 2003a Potential predictability of the Madden–Julian oscillation. *Bull. Am. Meteorol. Soc.*, **84**, 33–50

Waliser, D. E., Jin, K., Kang, I. S., Stern, W. F., Schubert, S. D., Lau, K. M., Lee, M. I., Shukla, J., Krishnamurthy, V., Satyan, V., Kitoh, A., Meehl, G. A., Galin, V. Y., Wu, G. Liu, Y. and Park, C. K. 2003b AGCM simulations of intraseasonal variability associated with the Asian summer monsoon. *Clim. Dyn.*, in press

Walker, G. T. 1923 Correlation in seasonal variations of weather, VII. A preliminary study of world weather. *Mem. Indian Meteorol. Dept.*, **24**, 75–131

Walker, G. T.	1924	Correlation in seasonal variations of weather IV: A further study of world weather. *Mem. Indian Meteorol. Dept.*, **24**, 275–332
	1928	World weather, III. *Mem. R. Meteorol. Soc.*, **4**, 97–106
	1933	'Seasonal weather and its prediction'. Report 103 of the British Association for Advancement of Science (Reprinted as pp. 25–44 in Annual Smithsonian Institute for 1935)
Walker, G. T. and Bliss, E. W.	1932	World weather, V. *Mem. R. Meteorol. Soc.*, **4**, 53–84
Wang, B. and Rui, H.	1990	Synoptic climatology of transient tropical intraseasonal convection anomalies 1975–85. *Meteorol. Atmos. Phys.*, **44**, 43–61
Wang, B. and Xie, X. S.	1997	A model for the boreal summer intraseasonal oscillation. *J. Atmos. Sci.*, **54**, 72–86
	1998	Coupled modes of the warm pool climate system. Part 1: The role of air–sea interaction in maintaining the Madden–Julian oscillation. *J. Climate*, **11**, 2116–2135
Weare, B. C. and Nasstrom, J. S.	1982	Examples of extended empirical orthogonal function analyses. *Mon. Weather Rev.*, **110**, 481–485
Webster, P. J., Magana, V. O., Palmer, T. N., Shukla, J., Tomas, R. A., Yanai, M. and Yasunari, T.	1998	Monsoons: Processes, predictability, and the prospects for prediction. *J. Geophys. Res.-Oceans*, **103**, 14451–14510
Wheeler, M. and Weickmann, K. M.	2001	Real-time monitoring and prediction of modes of coherent synoptic to intraseasonal tropical variability. *Mon. Weather Rev.*, **129**, 2677–2694
Xie, P. P. and Arkin, P. A.	1997	Global precipitation: A 17-year monthly analysis based on gauge observations, satellite estimates, and numerical model outputs. *Bull. Am. Meteorol. Soc.*, **78**, 2539–2558
Xue, Y., Sellers, P. J., Kinter, J. L. and Shukla, J.	1991	A simplified biosphere model for global climate studies. *J. Climate*, **4**, 345–364
Yang, X. Q., Anderson, J. L. and Stern, W. F.	1998	Reproducible forced modes in AGCM ensemble integrations and potential predictability of atmospheric seasonal variations in the extratropics. *J. Climate*, **11**, 2942–2959
Yasunari, T.	1979	Cloudiness fluctuations associated with the northern hemisphere summer monsoon. *J. Meteorol. Soc. Jpn*, **57**, 227–242
	1980	A quasi-stationary appearance of the 30–40 day period in the cloudiness fluctuations during the summer monsoon over India. *J. Meteorol. Soc. Jpn*, **59**, 336–354